

Grain boundary segregation prediction with a dual-solute model

Zuoyong Zhang and Chuang Deng*

Department of Mechanical Engineering, University of Manitoba, Winnipeg, Canada MB R3T 5V6

* Corresponding author: Chuang.Deng@umanitoba.ca

Abstract

Solute segregation along grain boundaries (GBs) profoundly affects their thermodynamic and kinetic behavior in polycrystalline materials. Recently, it has become a promising strategy for alloy design, mitigating grain growth by reducing excess GB energy and strengthening the GB network in nanocrystalline metals. In this context, the spectrum approach has emerged as a powerful tool to predict GB segregation. However, previous GB segregation predictions using this method relied heavily on single-solute segregation spectra, neglecting the crucial role of solute-solute interactions, which are often incorporated through a fitting parameter. In this work, we developed a dual-solute model whose segregation energy spectrum intrinsically considers the solute-solute interactions. Further improvement was made by describing the volume fraction of GBs as a varying parameter that scales with the total solute concentration and temperature. The refined dual-solute model was attempted to predict the GB segregation at finite temperatures in several binary systems. It shows significant improvement over the single-solute model and can accurately predict the hybrid Molecular Dynamics/Monte Carlo data within a broad temperature range with varying solute concentrations before forming secondary phases. This dual-solute model provides an effective way to statistically predict GB segregation with considerable accuracy in nanocrystalline metals.

Keywords:

Grain boundary segregation; Atomistic simulations; Dual-solute model; Segregation energy spectrum

1. Introduction

In polycrystalline metals, fine-grained structures usually exhibit superior mechanical properties compared to their coarse-grained counterparts due to the renowned Hall-Petch strengthening [1–3]. However, these fine structures are often unstable and encounter grain coarsening which can be

attributed to the high excess grain boundary (GB) energy that significantly increases the driving force for grain growth in nanocrystalline (NC) metals [4–7]. During the past decades, significant efforts have been made to explore how to stabilize the fine-grained structures and hinder grain coarsening. In this context, solute segregation at GBs has become a promising alloy design tool against grain growth by lowering the excess GB energy and stabilizing the GB network in NC metals [8–14]. Therefore, to effectively manage the process, it is imperative to gain a thorough understanding of the fundamental physics underlying segregation phenomena.

To predict GB segregation behavior, the GB segregation energy serves as a crucial parameter for influencing the likelihood of solute segregation, and that is, negative values indicate a tendency for solute segregation towards GB regions, while positive values suggest the opposite [12,13]. In the early days, the McLean-type approaches [12,15] treated each GB site possessing the same environment with the identical energy, and the solute segregation driving force was described with a single average segregation enthalpy. In the Fowler-Guggenheim [16] (F-G) model, a solute-solute interaction component was added to the adsorption energy as a correction for higher solute concentrations. Nevertheless, this separated component was mainly obtained by fitting experimental data [17,18], and still based on the average assumption [19]. Several empirical approaches were then developed to describe the segregation energy, such as the Hondros-Seah [20] and Miedema-based ones [21–23]. These classical approaches are very useful for alloy design with plentiful empirical data available to select alloying species [12]. However, the large variations of local atomic environments [24–26] were missing from these approaches due to the average assumption, which may cause significant deviations in GB segregation prediction [27].

A spectral approach, proposed to address the limitations of classical approaches characterized by oversimplification, has garnered significant attention. It can be dated back to 1977 by White and Coghlan [28] who explained the energetic driving force of GB segregation by demonstrating the spectral nature of segregation binding energy. Recently, inspired by the studies of White and Stein [29] and Kirchheim [30,31], Wagih and Schuh [32] developed the spectral approach and proposed a skew-normal model to describe the site-wise nature of GB segregation energy. A number of GB segregation energy spectra have been calculated using machine learning techniques by Wagih and

Schuh [33,34] providing a basic understanding of the segregation tendency of numerous binary systems.

Since then, there has been significant interest in the spectral approach. Tuchinda and Schuh explored the strong grain size dependencies of solute segregation preference [35] and the triple junction effects on the GB segregation spectra [36]. Then, they calculated the vibrational entropy spectrum for various binary systems and revealed the strong linear correlation between site segregation energy and vibrational entropy [37]. By investigating the hydrostatic pressure effects on GB segregation spectra, Zhang and Deng [38] demonstrated that such effects can either enhance or hinder the solute segregation tendencies depending on the alloy systems. Furthermore, they observed a noteworthy transition in segregation tendencies within certain alloy systems, attributable to the changes in the elastic component induced by hydrostatic pressure. Furthermore, Matson and Schuh [39] developed a framework to construct a phase-and-defect diagram based on the spectral GB segregation. On the basis of the spectral segregation energy concept, Pal et al. [24] also investigated the spectrum of atomic excess free volume in GBs, elucidating the spectral nature of segregation energy from a structure-property correlation aspect.

However, prior GB segregation prediction using the segregation spectrum was only applicable for dilute conditions due to the absence of solute-solute interaction component of segregation energy which may significantly influence the segregation behavior [26,40–42]. To address this issue, two different approaches were developed to incorporate the solute-solute interactions into the skew-normal model: (i) linear approximation which adds a fitting parameter as the solute-solute interaction component [43]; (ii) atomistic approach which utilizes atomistic simulations to directly measure the solute-solute interactions [44]. The former added a correction to the segregation energy to describe the contribution of solute-solute interactions by fitting the hybrid Monte Carlo/Molecular Statics (MC/MS) results using the F-G model. To eliminate the dependence on fitting parameters, the latter employed atomistic simulations to measure the solute-solute interactions explicitly for each GB site based on its coordination number and the bonding energies with its nearest neighbors, which were in excellent agreement with the results obtained by hybrid MC/MS simulations.

Nevertheless, the GB network was assumed to be static at 0 K in the previous models, while, in

realistic materials, the GBs may thicken as more solutes segregate or evolve significantly simply due to thermal effects at finite temperatures. Moreover, previous models consider the solute-solute interactions not intrinsically but separately with the segregation energies. Therefore, there is an urgent need for a novel model capable of integrating the solute-solute interaction information into the segregation energy spectrum, enabling accurate prediction of GB segregation at finite temperatures.

In this study, we aim to improve the segregation prediction by introducing a dual-solute (DS) segregation framework for computing GB segregation energy spectrum. The main assumption is that, unless for systems with negligible solute-solute interactions, the energy states that a solute can access would be dramatically changed due to the presence of pre-existing solutes, leading to significant alteration of the shape and position of the segregation energy spectra. Furthermore, one can also explicitly quantify the solute-solute interactions by comparing the segregation energy spectra based on the single- and dual-solute models. To validate these assumptions, the segregation energy spectra were utilized to assess solute-solute interactions and forecast GB segregation in various binary systems, indicating the reliability of the DS model in predicting GB segregation.

2. Thermodynamics of grain boundary segregation

2.1. Interpretation of segregation energy

It is worth noting that comprehensive thermodynamics treatment [45] is the crucial start point for the discussions of GB segregation isotherms throughout the paper. Hence, the solute segregation energy should be interpreted as the change of free energy, i.e., ΔG^{seg} , between after and before segregation of a solute:

$$\Delta G^{\text{seg}} = \Delta H^{\text{seg}} - T\Delta S_{\text{vib}}^{\text{seg}} \quad (1)$$

where T is the system temperature and $\Delta S_{\text{vib}}^{\text{seg}}$ is the excess vibrational entropy of segregation [46]; the segregation enthalpy ΔH^{seg} is given by:

$$\Delta H^{\text{seg}} = \Delta E^{\text{seg}} - P\Delta V \quad (2)$$

where ΔE^{seg} refers to the segregation internal energy; $P\Delta V$ indicates the work done by the pressure

P caused by change in volume ΔV . In this work, some necessary simplifications are made as follows: (i) we focus on the segregation phenomenon in solids, where the $P\Delta V$ component is negligible [47] when the pressure P is precisely controlled at 0 bar using the Parrinello–Rahman algorithm [48] like what we have done in our previous work [38]; (ii) the segregation energies will be calculated at 0 K using the conjugate gradient (CG) minimization, indicating the negligible contribution of the excess vibrational entropy component. Thus, the segregation free energy can be approximated as [32–34,43,44]:

$$\Delta G^{\text{seg}} \approx \Delta E^{\text{seg}} \quad (3)$$

2.2. Classical segregation isotherms

One of the most important classical approaches to predict GB segregation is the renowned McLean isotherm [15], where the atomic sites in the polycrystal are divided into two types, e.g., bulk (grain interior) and GB sites, and expressed as:

$$\frac{\bar{X}^{\text{gb}}}{1-\bar{X}^{\text{gb}}} = \frac{X^{\text{c}}}{1-X^{\text{c}}} \exp\left(-\frac{\Delta \bar{E}^{\text{seg}}}{\kappa_{\text{B}} T}\right) \quad (4)$$

where \bar{X}^{gb} is the average solute concentration at GBs, while X^{c} indicates the solute concentration at bulk regions; κ_{B} refers to the Boltzmann constant; and the average segregation energy, $\Delta \bar{E}^{\text{seg}}$, is evaluated as:

$$\bar{E}^{\text{seg}} = E_{\text{solute}}^{\text{gb}} - E_{\text{solute}}^{\text{c}} \quad (5)$$

where $E_{\text{solute}}^{\text{gb}}$ and $E_{\text{solute}}^{\text{c}}$ are the system energies when a solute is sitting at a GB site and bulk site, respectively. For a given system with finite grain sizes and total solute concentrations (X^{tot}), both volume fractions for GB (f^{gb}) and bulk (f^{c}) become finite, where $f^{\text{gb}} + f^{\text{c}} = 1$, and follow the relationship according to the rule of mixture [49]:

$$X^{\text{tot}} = (1 - f^{\text{gb}})X^{\text{c}} + f^{\text{gb}}\bar{X}^{\text{gb}} \quad (6)$$

Thus, \bar{X}^{gb} can be directly solved for a fixed X^{tot} in a finite polycrystalline model. However, it

always fails to predict GB segregation when the solute concentration is beyond dilute limit [27].

GB segregation may show solute concentration dependence when X^{tot} is beyond dilute limit. To explain this phenomenon, the F-G model [16] added a solute-solute interaction component ($\omega\bar{X}^{\text{gb}}$) into the average segregation energy:

$$\frac{\bar{X}^{\text{gb}}}{1-\bar{X}^{\text{gb}}} = \frac{X^{\text{c}}}{1-X^{\text{c}}} \exp\left(-\frac{\Delta\bar{E}^{\text{seg}} + \omega\bar{X}^{\text{gb}}}{\kappa_{\text{B}}T}\right) \quad (7)$$

where ω is the interaction term. Apparently, the solute-solute interaction component increases with the solute concentration at GBs, i.e., \bar{X}^{gb} .

As aforementioned, the classical isotherms treat the GB regions as an entity and use a single average energy term to account for evaluation of GB segregation tendency. This simplification excludes the significance of local environment variations, and therefore, may cause large errors in predicting GB segregation, especially when the solute concentration is on higher level [27,43].

2.3. The spectral approach

Compared to the classical approaches, the spectral approach suggests that each GB site i has its own segregation energy ΔE_i^{seg} with a particular probability F_i^{seg} [32], due to the unique local environment:

$$F_i^{\text{gb}} = \frac{1}{\sqrt{2\pi}\sigma} \exp\left[-\frac{(\Delta E_i^{\text{seg}} - \mu)^2}{2\sigma^2}\right] \text{erfc}\left[-\frac{\alpha(\Delta E_i^{\text{seg}} - \mu)}{\sqrt{2}\sigma}\right] \quad (8)$$

where α , μ , and σ are three fitting parameters referring to the shape, characteristic energy, and width of the skew-normal distribution, respectively. Similar to the form of McLean-type model, the spectral GB segregation prediction model without solute-solute interactions can be expressed as [32]:

$$X^{\text{tot}} = (1 - f^{\text{gb}})X^{\text{c}} + f^{\text{gb}} \int_{-\infty}^{\infty} F_i^{\text{gb}} \left[1 + \frac{1-X^{\text{c}}}{X^{\text{c}}} \exp\left(\frac{\Delta E_i^{\text{seg}}}{\kappa_{\text{B}}T}\right)\right] d\Delta E_i^{\text{seg}} \quad (9)$$

To incorporate the solute-solute interaction contribution, Wagih and Schuh [43] added an interaction term ΔE^{ω} by following the F-G method [16]:

$$X^{\text{tot}} = (1 - f^{\text{gb}})X^{\text{c}} + f^{\text{gb}} \int_{-\infty}^{\infty} F_i^{\text{gb}} \left[1 + \frac{1-X^{\text{c}}}{X^{\text{c}}} \exp \left(\frac{\Delta E_i^{\text{seg}} + \Delta E^{\omega}}{\kappa_{\text{B}} T} \right) \right] d\Delta E_i^{\text{seg}} \quad (10)$$

However, the ΔE^{ω} in Eq. (10) is obtained by fitting the hybrid MC/MS data using the F-G model, which is not derived from the physical properties directly. Thereafter, Matson and Schuh [44] proposed an atomistic method to assess the solute-solute interactions on atomistic-level:

$$X^{\text{tot}} = (1 - f^{\text{gb}})X^{\text{c}} + f^{\text{gb}} \int_{-\infty}^{\infty} F_i^{\text{gb}} \left[1 + \frac{1-X^{\text{c}}}{X^{\text{c}}} \exp \left(\frac{\Delta E_i^{\text{seg}} - 2\bar{\Omega}^{\text{gb}}\bar{X}^{\text{gb}} + 2\Omega^{\text{c}}X^{\text{c}}}{\kappa_{\text{B}} T} \right) \right] d\Delta E_i^{\text{seg}} \quad (11)$$

where $\bar{\Omega}^{\text{gb}}$ and Ω^{c} are average heat of mixing parameters of the GB and bulk regions, respectively, which are derived from atomistic simulations by evaluating the possible bonding energies of a solute atom with its nearest neighbors at the corresponding sites. This approach eliminates the need for fitting parameters but requires extra simulations that exhaust every GB site, which is a non-trivial task. In the following, we present the dual-solute segregation framework that intrinsically embeds the solute-solute interactions.

3. Dual-solute segregation framework

3.1. Volume fraction of GBs

In a closed system with finite grain sizes, the atomic sites as an entity are shared by GB and bulk regions. It is reported that the volume fraction of GBs is a function of the average grain size (d) and GB thickness (t) $f^{\text{gb}} = 1 - [(d - t)/d]^3$ [11]. However, for a given closed system, the GB thickness may not be a constant, but show a solute concentration dependence after segregation [50–53]. Kim and Park [50] observed that segregation can slightly change the GB width coupling with reduction in GB energy. Chen et al. [51] reported that the width of the Mg atomic concentration peak, i.e., Mg segregated GB region, increased from 5 nm in Al-4Mg alloy to 10 nm in Al-8Mg alloy after segregation. The much thicker segregation zone vs. expected structural GB width also indicates the potential solute segregation at near GB regions and thus thickens the GBs [52,53]. These findings signify the inevitable solute effects on GB volume fractions. Thus, for a given system with a fixed size, it is reasonable to assume that the GB volume fraction is a function of total solute concentration:

$$f^{\text{gb}} = m + nX^{\text{tot}} + r(X^{\text{tot}})^2 \quad (12)$$

where m , n , and r are parameters by fitting the hybrid MD/MC results. f^{gb} may exhibit potential or alloy system dependencies, which may or may not change with total solute concentration. The parameter m is necessarily finite, whereas n and r are not. For example, when both n and r are equal to zero, f^{gb} would be a fixed value concerning the total solute concentration.

3.2. Single-solute segregation

Prior GB segregation energy spectra are mostly obtained by the segregation energy iteration of a single-solute (SS) atom across the whole GB sites, i.e., dilute conditions without solute-solute interactions. The per-site segregation energy was evaluated by:

$$\Delta E_i^{\text{seg}} = E_i^{\text{solute}} - E_c^{\text{solute}} \quad (13)$$

where E_i^{solute} is the minimized system energy when a solute is located at a GB site i , while E_c^{solute} is the reference energy that is the reference energy when a solute is sitting at the chosen bulk site which is the center of the largest grain to avoid the elastic interactions with GBs [32,44]. Eq. (13) has been widely used for GB segregation energy spectrum calculations [32–34,43,44].

3.3. Dual-solute segregation

In this study, we developed a DS segregation framework which is used to consider the solute-solute interactions in a straightforward manner. Similar to the SS segregation, we first identified all the GB sites and their corresponding nearest neighbors of the thermally relaxed NC metals. Then, we constructed a neighbor-list consisting of pairs of all GB sites and their neighbors without duplication. For instance, in this list, GB site A and one of its neighbors B can form A-B pair which is identical to the B-A pair that one of them will be removed from the list. The i th DS segregation energy in the neighbor-list, ΔE_i^{DS} , is calculated by:

$$\Delta E_i^{\text{DS}} = E_{j+k}^{\text{gb}} - E_0 - 2\Delta E^{\text{r}} \quad (14)$$

where E_{j+k}^{gb} is the minimized system energy at 0 K when the GB site j and one of its nearest neighbors k are occupied by two solute atoms. The site k can be a GB or near GB site indicating that not only

GB sites but also near GB sites can be potentially segregated by solute atoms. The term E_0 refers to the system energy of a pure metal NC model after full relaxation and minimization, while ΔE^r is a reference energy evaluated by:

$$\Delta E^r = E_c^{\text{solute}} - E_0 \quad (15)$$

Therefore, we can obtain a discrete DS segregation spectrum which is like but different from the SS segregation energy spectrum resulting from Eq. (13). Compared to the segregation energy spectrum of the SS model, that of the DS model is no longer a per-site distribution, but a per-couple one.

Now, it is ready for GB segregation predictions. Herein, we employ both the SS and DS segregation energy spectra for GB segregation prediction with solute-solute interactions by following the expression similar to Eq. (10):

$$X^{\text{tot}} = (1 - f^{\text{gb}})X^c + f^{\text{gb}} \int_{-\infty}^{\infty} F_i^{\text{gb}} \left[1 + \frac{1-X^c}{X^c} \exp \left(\frac{\Delta E_i^{\text{DS}} + \Delta E_{\text{int}}^{\text{add}}}{\kappa_B T} \right) \right] d\Delta E_i^{\text{DS}} \quad (16)$$

where $\xi \Delta E^\mu$ is used to represent the additional solute-solute interactions ($\Delta E_{\text{int}}^{\text{add}}$), in which ΔE^μ is the difference between the characteristic energies for the DS segregation energy spectrum (μ_{DS}) and SS segregation energy spectrum (μ_{SS}), which reflects the shift in segregation energy spectra resulting from the solute-solute interactions within the DS model:

$$\Delta E^\mu = \mu_{\text{DS}} - \mu_{\text{SS}} \quad (17)$$

and ξ represents an interaction correction coefficient within the DS model. This coefficient accounts for the fact that the DS model exclusively considers interactions between the two closest solutes while neglecting potential short- and long-range solute-solute interactions. Thus, it is necessary to enhance the additional solute-solute interactions by evaluating ξ in the following manner:

$$\xi = \frac{\alpha_{\text{DS}}}{\alpha_{\text{SS}}} \cdot \frac{\sigma_{\text{DS}}}{\sigma_{\text{SS}}} \quad (18)$$

where α_{SS} , σ_{SS} , α_{DS} , and σ_{DS} are the parameters obtained by fitting the SS and DS segregation energy spectra using Eq. (8), respectively. Apparently, α_{SS} and σ_{SS} must be finite. Thereafter,

combining with Eqs. (12), (17), and (18), Eq. (16) can be numerically solved for total solute concentration (X^{tot}) with respect to bulk solute concentration (X^c) after segregation, and so can be the volume fraction of GBs (f^{gb}). Finally, the solute concentration at GBs (\bar{X}^{gb}) can be derived from Eq. (6).

4. Simulation methods

4.1. The determination of segregation energies

The selection of binary systems follows the three criteria: (i) the existence of reliable interatomic potentials; (ii) spectral data availability for comparison in the literature [32,33,43]; (iii) representative binaries with weak or strong solute-solute interactions. Accordingly, the Al-Mg system was chosen due to the weak repulsion among solutes [43] and extensive interest in its segregation spectra [32,33,38,43,44]; the Ag-Ni and Ag-Cu systems were selected for the strong attractions among solutes and the tendency of forming small solute clusters [54–56], indicating the attractive solute-solute interactions; the Al-Ni system was employed because of the large size mismatch between solvent and solute. In this work, we choose the NC structures with randomly generated grains as the study specimens due to their complexity in local atomic environments, which cannot be fully captured by special GBs [57]. The fully relaxed NC-Al ((16 nm)³) and -Ag ((20 nm)³) specimens with randomly oriented grains, used for segregation energy calculations in this study, were provided by Wagih and Schuh from their previous studies [32,33].

In this work, the Large-scale Atomic/Molecular Massively Parallel Simulator (LAMMPS) software package [58] was employed to perform all atomistic simulations. OVITO [59] was used for visualization and structural analysis. The additive-common neighbor analysis method [60] was used to identify non-face-centered cubic (FCC) atoms, which were all assigned as GB sites. The interatomic interactions in each binary system were characterized using the embedded atom method (EAM) [61] potentials, which were specifically developed for Al-Mg [62], Ag-Ni [63], Ag-Cu [64], and Al-Ni [65], respectively. Those EAM potentials have been extensively used in the investigation of segregation in their respective binary systems, yielding reliable results [26,32,38,43,54,55]. Then, MS simulations were conducted, and the segregation energies were calculated using Eqs. (13) and

(14) for the SS and DS models, respectively.

4.2. Hybrid MD/MC simulations

To assess the accuracy of the DS prediction model, hybrid MD/MC simulations were conducted using LAMMPS to obtain the segregated structures at finite temperatures. The simulations were carried out employing a variance-constrained semi-grand-canonical (VC-SGC) ensemble [66], following the procedures described in Refs. [54,55]. MC trials were performed with three constant parameters, i.e., the total solute concentration c_0 , the chemical potential between the solvent and the solute species $\Delta\mu_0$, and the variance constraint κ . We used test runs to determine the proper $\Delta\mu_0$ to obtain the desired solute concentration, i.e., c_0 , with $\kappa = 1000$, which was conducted for all binary systems at 300 K. The optimized parameters are listed in Supplementary Tables 1-4.

The hybrid MD/MC simulations were performed for all alloy systems at desired solute concentrations. The timestep was consistently set to 2 fs throughout each hybrid MD/MC simulation. All the NC structures were first minimized using the CG algorithm. Then, they were relaxed using the isothermal-isobaric ensemble (NPT) under zero-pressure at 300 K for 200 ps. Thereafter, in each MC cycle, the number of trial moves was set to 10% of the total atoms in the system, with a total of 40,000 MC cycles conducted at 300 K. Additionally, each MC cycle was separated by 10 MD steps at the same temperature to facilitate the structural relaxation after the atomic moves and chemical mixing, where the temperature was controlled using the canonical ensemble (NVT) and the pressure was precisely maintained to 0 bar by a Berendsen barostat. Following this, each NC structure was again relaxed under zero-pressure at 300 K using the NPT ensemble for 200 ps, then gradually cooled to 0 K with a constant rate of 3 K/ps. Finally, each NC structure was energetically minimized using the CG algorithm with the pressure kept at 0 bar using the Parrinello–Rahman method [48].

4.3. Size and temperature effects

The solute content at GBs may also be affected by the size of the NC structures by tuning the GB volume fraction [11]. Therefore, another large NC-Al ((40 nm)³) (L-NC-Al) was generated using the random Voronoi tessellation with the toolkit AtomsK [67], followed by a thermal relaxation

procedure: first, annealing the NC-Al model using the Nose-Hoover thermostat/barostat under 0 bar at 500 K for 500 ps; then, gradually cooling the NC model to 0 K with a constant rate of 3 K/ps, followed by an energy minimization using the CG algorithm. The annealed L-NC-Al has 18 randomly oriented grains with the average grain size of 15 nm and ~ 3853400 atoms. Subsequently, it was employed for hybrid MD/MC simulations, utilizing the same parameters as those of the Al-Mg $((16 \text{ nm})^3)$ polycrystal at 300 K, to evaluate the size effect on the accuracy of the DS prediction model.

Furthermore, it has been reported that temperature can significantly influence the segregation behaviors of solutes, with higher temperatures leading to lower solute concentrations at GBs [43]. Herein, we performed hybrid MD/MC simulations, as described previously, using the Al-Mg $((16 \text{ nm})^3)$ polycrystal at temperatures of 400 and 500 K, and the Ag-Ni system $((20 \text{ nm})^3)$ at 500 and 700 K, respectively. These were carried out to evaluate the potential effects of temperature on the accuracy of the DS prediction model. Test runs were also conducted to find out the optimized $\Delta\mu_0$ for each desired solute concentration and temperature. The resulting parameters are listed in Supplementary Tables 5-8.

5. Results

5.1. Segregation energy spectra

The thermally annealed NC-Al and -Ag GB networks are shown in Fig. 1(a) and (d), respectively. Grains are randomly oriented in both NC models which were employed to calculate the segregation energy distributions for both SS (Eq. (13)), and DS (Eq. (14)) models in Al-Mg, Al-Ni, Ag-Ni, and Ag-Cu, respectively. The best fitting parameters using the skew-normal distribution, i.e., Eq. (8), for the SS model in the Al-Mg system are $\alpha_{SS} = -1.5$, $\mu_{SS} = 11.6 \text{ kJ/mol}$, and $\sigma_{SS} = 20.5 \text{ kJ/mol}$, as shown in Fig. 1(b). This distribution matches a larger NC-Al with the size of $(36 \text{ nm})^3$ [32] and a smaller one with the size of $(10 \text{ nm})^3$ [44]. Moreover, the SS spectra for the Al-Ni, Ag-Ni, and Ag-Cu binaries are consistent with that of the segregation energy database [33], indicating the reliability of the segregation energy calculation method.

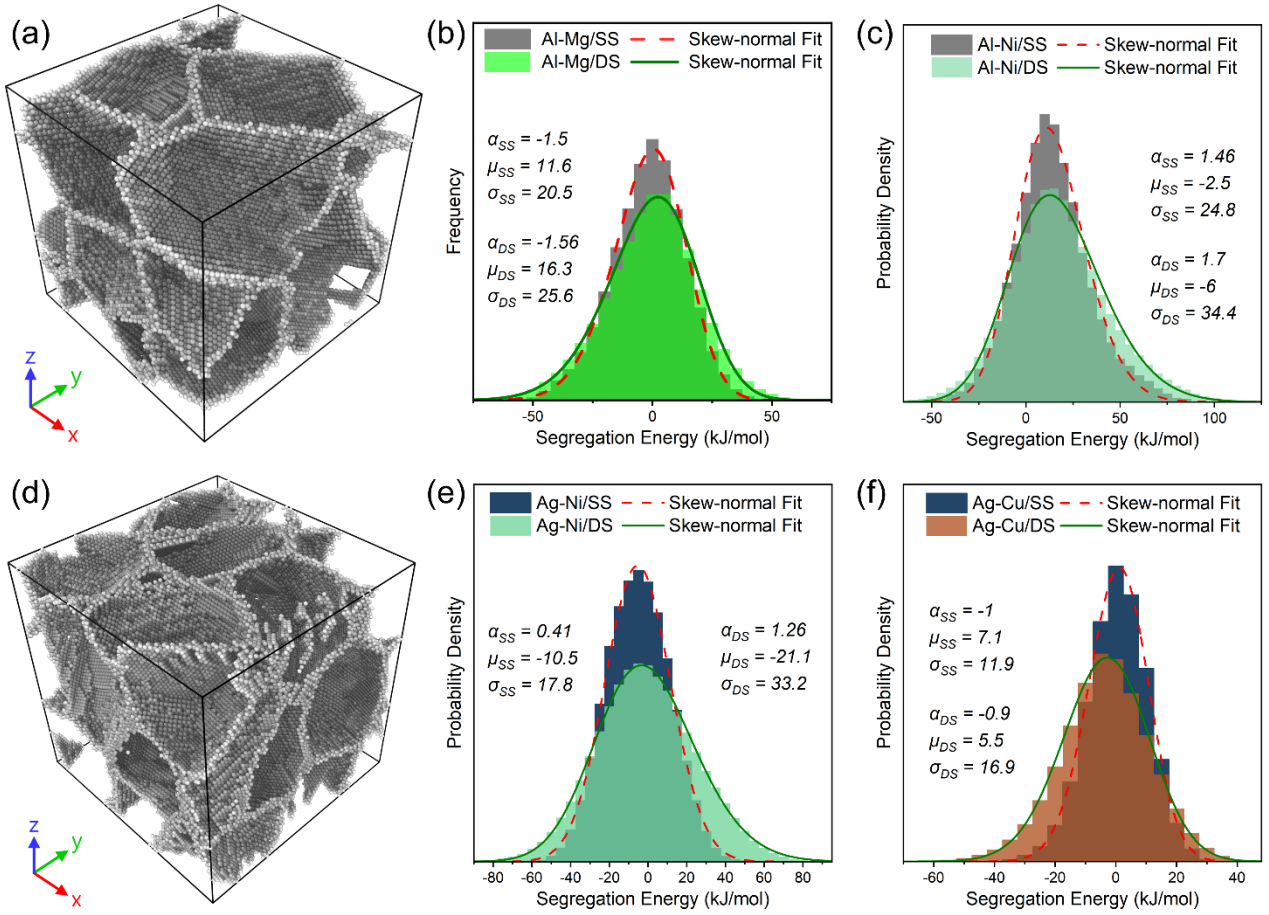


Fig. 1 GB networks of the fully relaxed (a) NC-Al ($16 \times 16 \times 16 \text{ nm}^3$) with 10 grains of an average grain size of 7 nm, and (d) NC-Ag ($20 \times 20 \times 20 \text{ nm}^3$) with 16 grains of an average grain size of 8 nm. The calculated SS and DS segregation energy spectra with the best fitted skew-normal distribution using Eq. (8) for the (b) Al-Mg, (c) Al-Ni, (e) Ag-Ni, and (f) Ag-Cu binaries, respectively.

The DS spectra displayed in Fig. 1 were plotted using the same bin size with that of the corresponding SS spectra. Significant changes in the shape and position of the DS spectra can be observed in each alloy system compared to the SS spectra. Each DS spectrum exhibits wider but lower peak probability density than its SS counterpart. This indicates that the segregation energy with solute-solute interactions varies in a larger range and more scattered, while the SS segregation energy seems more concentrated in a narrow range. For example, the DS segregation energy in Al-Mg ranges from -100 to 80 kJ/mol, which is much wider than that of SS segregation energy only ranging from -60 to 55 kJ/mol. This can also be interpreted by the larger σ_{DS} values compared to σ_{SS} . It is worth noting that the DS segregation energy is no more a site-wise but a pair-wise parameter assessing the energy difference of a pair of nearest neighbors which may adjacent GB atoms. The amount of distinct neighbor pairs is about nine times of that of GB sites which is the data size of the SS segregation

energy. This may account for the larger σ values of the DS spectra.

The fitting parameter α refers to the shape of the segregation energy spectrum, which indicates the skew direction of the spectrum: positive α means that the spectrum skews to the left, i.e., more negative energies, and vice versa. The α_{DS} has the same sign with its corresponding α_{SS} in each system, indicating that the solute-solute interactions in the DS model are not strong enough to alter the shape of the spectrum. Accordingly, the parameter μ is the characteristic energy of the spectrum. The greater μ_{DS} than μ_{SS} in the same system is considered as an indicator of the repulsive solute-solute interactions, while the smaller μ_{DS} means solute-solute attractions. For instance, in the Al-Mg system, the $\mu_{DS} = 16.3$ kJ/mol is larger than the $\mu_{SS} = 11.6$ kJ/mol, as shown in Fig. 1(b). This means that the segregation energy of the DS model tends to be more positive, suggesting the solute-solute repulsion, which has been reported by atomistic studies in the Al-Mg system [43,44]. However, the smaller μ_{DS} than μ_{SS} can be observed in the other three systems, as shown in Fig. 1(c), (e), and (f), speaking the solute-solute attraction, which can be confirmed by the formation of solute clusters in the Ag-Ni [54,55] and Ag-Cu [56] systems.

5.2. Volume fraction of GBs

Before discussing the changes in GB volume fraction, it is necessary to demonstrate the changes in structure and solute distribution of the large Al-Mg polycrystal with different solute concentrations after hybrid MD/MC simulations at 300 K, as shown in Fig. 2. Almost all the solute atoms segregate to GBs when Mg content is 1 at.%, as shown in Fig. 2(a), indicating the strong segregation tendency of Mg solutes in Al at this condition. Fig. 2(b) shows that many Mg atoms are dispersed inside the grains. Meanwhile, Mg solutes are also concentrated in GB regions. Increasing the Mg content to 7 at.%, extremely concentrated Mg atoms at GBs can be observed in Fig. 2(c). However, the solute concentration at GBs decreased significantly at GB regions at Al-Mg 8 at.%. Moreover, highly ordered structures can be seen in grain interiors with an FCC structure, suggesting the formation of secondary phases, e.g., the circled regions with red ellipses, as shown in Fig. 2(d), which is consistent with experimental studies [68,69]. The Al-Mg 16 nm polycrystal also exhibits the same behaviors after hybrid MD/MC simulations.

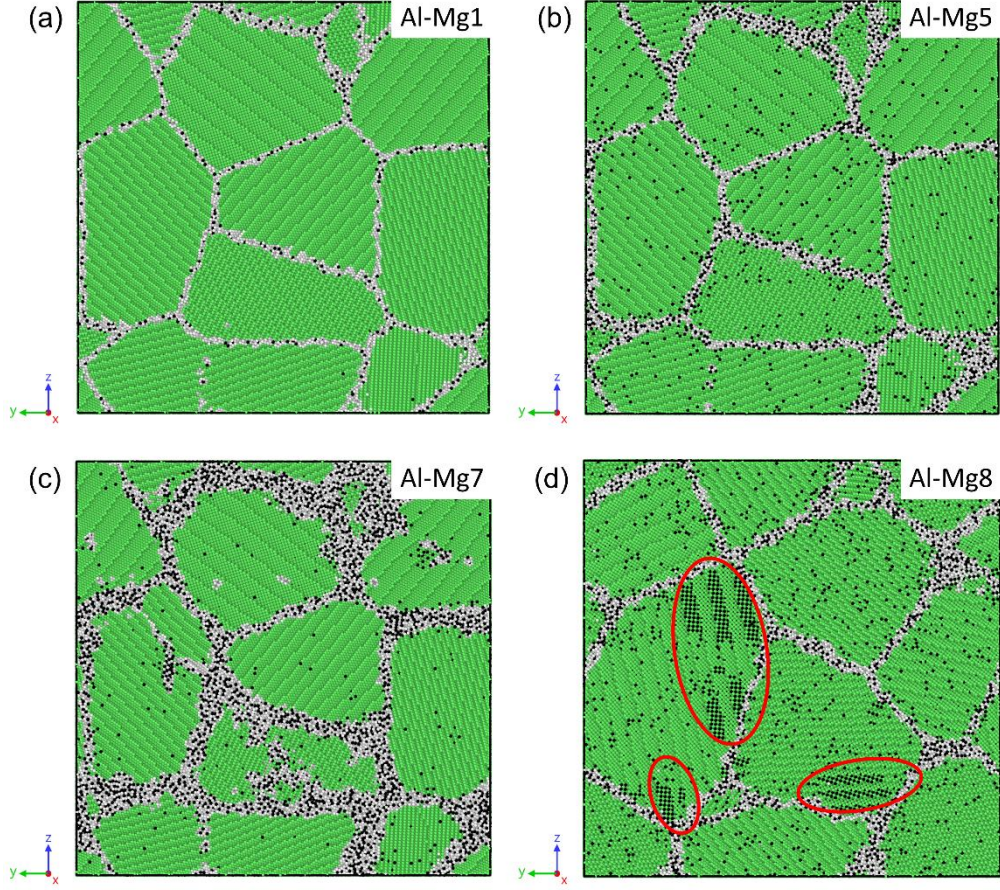


Fig. 2 The structures and solute distributions of the Al-Mg system with the dimension of $40 \times 40 \times 40 \text{ nm}^3$ at different Mg concentrations after hybrid MD/MC simulations at 300 K: (a) Al-Mg 1 at.%, (b) Al-Mg 5 at.%, (b) Al-Mg 7 at.%, and (b) Al-Mg 10 at.%. The green spheres are fcc atoms while the gray ones represent the GB atoms. The dark spheres are the solute atoms.

Fig. 2 also reveals an evident thickening phenomenon of GBs with increasing solute concentrations in Al-Mg after hybrid MD/MC simulations. This indicates that the volume fraction of GBs is a function of total solute concentrations. At 7 at.% Mg concentration, a critical point is reached in the Al-Mg system with the thickest GBs among the examined Mg concentrations. At this concentration, the GB structures experience significant changes following the extreme adsorption of Mg atoms into the GB regions, as illustrated in Fig. 2(c). Once forming the secondary phase at Mg 8 at.%, the GBs become thinner compared to the Mg-7 at.% condition, as shown in Fig. 2(d). In the meantime, more Mg atoms can be observed in bulk regions but with ordering distribution. They were probably swapped back to bulk regions to facilitate the formation of secondary phases and reduce the interfacial energy [70]. Furthermore, these ordered structures are adjacent to GBs, indicating that they start growing from GB regions. The reduction in solute content at GBs suggests that there might be a

competition between the segregation of solute atoms at GBs and formation of secondary phases in Al matrix [71].

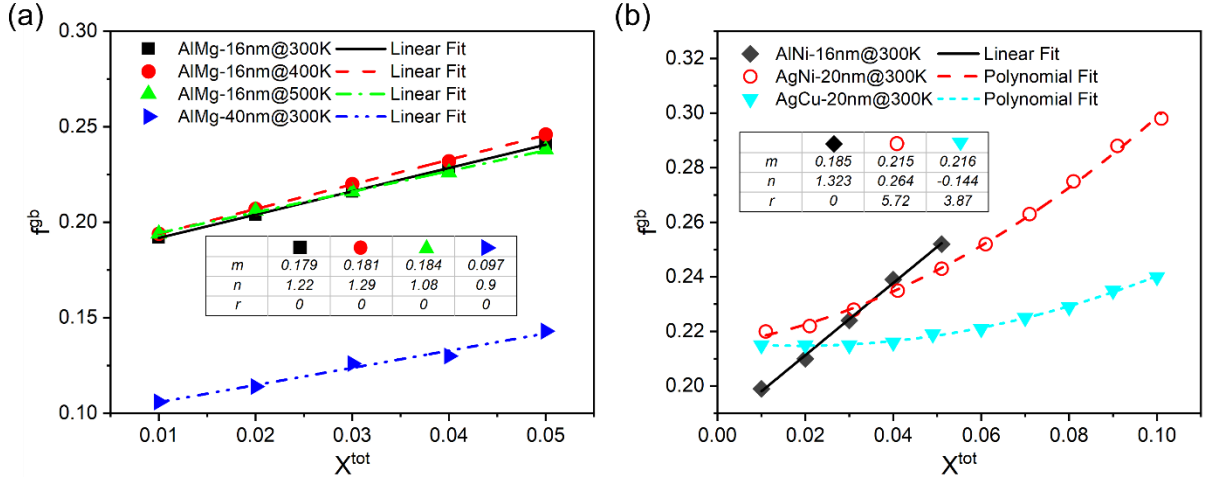


Fig. 3 (a) GB volume fractions in the Al-Mg system at different temperatures, sizes, and total solute concentrations. (b) GB volume fractions in the Al-Ni, Ag-Ni, and Ag-Cu systems with different solute concentrations at 300 K. The inset tables in (a) and (b) are the fitting parameters using the Eq. (12).

In this study, the GB volume fraction f^{gb} was evaluated using the atomic fraction of GB regions [32,43]. It is known that the GB volume fraction f^{gb} is a function of grain size and GB thickness [11]. Most of the previous studies treated f^{gb} as a constant due to the static features of GBs during hybrid MC/MS simulations [43,44]. Herein, we show that f^{gb} is a function of total solute concentration (X^{tot}) since the GBs were significantly thickened by solute segregation. Therefore, the GB thickness is no longer constant, indicating that, for a given polycrystal with finite size, the GB volume fraction varies with solute concentrations. The correlation between f^{gb} and X^{tot} can be seen in Fig. 3. In Al-Mg, the GB volume fraction is linearly correlated with the total solute concentration at different temperatures and sizes, as shown in Fig. 3(a). It also shows that f^{gb} is sensitive to model size but scarcely influenced by temperature. In the Al-Mg 16 nm model, only minor variations are observed in the slopes (n) and interceptions (m) of the linear fit when increasing temperature from 300 to 500 K. Thus, it is reasonable to apply the parameters of 300 K to represent the other temperature conditions. Nevertheless, changes in model sizes can dramatically alter the fitting parameters, as illustrated by the parameters for the Al-Mg 40 nm model in Fig. 3(a). Similarly, the f^{gb} in Al-Ni also exhibits a linear correlation with the total solute concentration, as shown in Fig.

3(b). However, the f^{gb} in Ag-Ni and Ag-Cu systems shows a polynomial correlation with their total solute concentrations at 300 K. Therefore, the parameter " r " becomes finite in both Ag-Ni and Ag-Cu systems, whereas it remains zero in Al-based systems.

6. Grain boundary segregation prediction

With all the data in hand, our focus now shifts to validating the DS model, represented by Eq. (16). In this section, we focus on the 300 K conditions. The results obtained from hybrid MD/MC simulations at 300 K will serve as the benchmark for examining the prediction accuracy. Our initial attention is on segregation prediction in the Al-Mg system, where the solute-solute repulsion was observed in the previous section, using the DS model. We will compare the results with those obtained using other models, such as the McLean isotherm and the spectral model based on the SS spectrum. Next, we aim to extend the DS prediction model to other systems where the solute-solute attraction was identified, such as Al-Ni, Ag-Ni, and Ag-Cu.

6.1. Solute-solute repulsion

The “real” segregation state was obtained by the hybrid MD/MC simulations at finite temperatures using the VC-SGC ensemble [66]. After segregation, each polycrystal was cooled to 0 K. So, these polycrystals can have a common basis for comparison. The GB solute concentration predicted using the classical McLean model exhibits a linear correlation with the total solute concentration [27,43,44], as shown in Fig. 4. It was obtained by solving Eq. (4) with the $\Delta\bar{E}^{seg} = -11.6$ kJ/mol which is the negative value of the characteristic segregation energy of the SS spectrum in Fig. 1(b). The negative value here is because of the minus sign in front of $\Delta\bar{E}^{seg}$ in Eq. (4). No solute-solute interactions were considered in this model. Thus, the prediction of \bar{X}^{gb} by the McLean model deviates far away from the hybrid MD/MC results when the total solute concentration is beyond the dilute limit [27,43,44], which can be observed from Fig. 4.

Table 1 Parameters of Al-Mg used for the DS prediction model, i.e., Eq. (16). The α , μ , and σ are obtained from fitting the SS and DS segregation energy spectra using the skew-normal distribution.

		α	μ , kJ/mol	σ , kJ/mol	ΔE^μ , kJ/mol	ζ	$\Delta E_{\text{int}}^{\text{add}}$, kJ/mol
Al-Mg	SS	-1.5	11.6	20.5	4.8	1.3	6.24
	DS	-1.56	16.3	25.6			

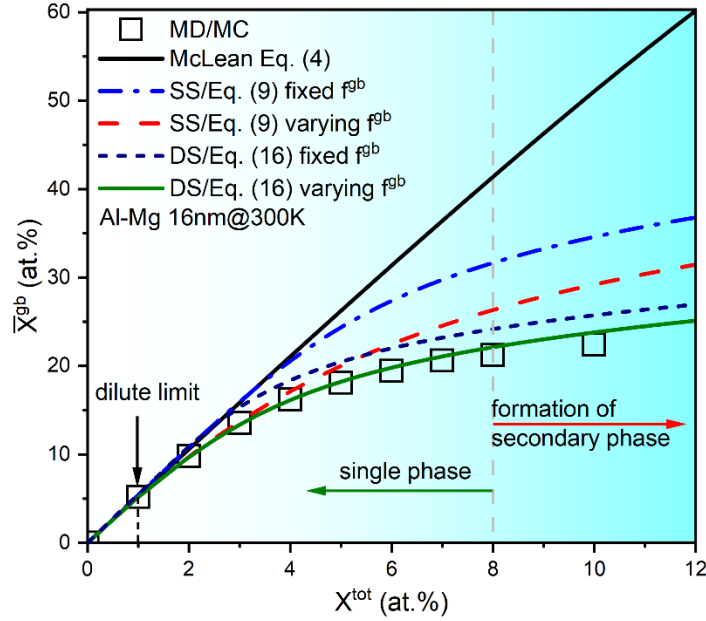


Fig. 4 Comparison of the DS prediction model Eq. (16) with others where solute-solute interactions are excluded, such as the McLean Eq. (4), the SS model Eq. (9), against the hybrid MD/MC simulations at 300 K in the Al-Mg 16 nm polycrystal. The contribution of f^{gb} was also incorporated with the fixed and varying values.

Following that, our focus shifts to the SS spectral prediction model. The blue dash dot and red dash curves in Fig. 4 represent the fitting results by solving the Eq. (9) with the SS spectrum fitting parameters of Al-Mg listed in Table 1. The difference is that the former curve is based on a constant $f^{\text{gb}} = 0.179$ which is the interception value, i.e., $m = 0.179$, $n = 0$, and $r = 0$ in Eq. (12), shown in Fig. 2(a), while the latter one is obtained by a variable f^{gb} which is a linear function of the total solute concentration with $m = 0.179$, $n = 1.22$, and $r = 0$ in Eq. (12). Compared to the constant f^{gb} curve, the curve with varying f^{gb} reveals better relative error against the real segregation state, i.e., \bar{X}^{gb} obtained from hybrid MD/MC, indicating the necessary of using the variable GB volume fraction. Nevertheless, there is still a dramatic deviation between the curve with varying f^{gb} and the real segregation state.

Further, the DS prediction curves are obtained by numerically solving Eq. (16) using the parameters listed in Table 1. The calculated solute-solute interaction energy is ~ 6.24 kJ/mol, which is much smaller than that of previous studies [43,44]. This is because the DS spectrum intrinsically contains information of solute-solute interactions. But this intrinsic information is not strong enough to describe the whole picture of solute-solute interactions. Thus, we need an additional interaction component, i.e., $\Delta E_{\text{int}}^{\text{add}}$, to overcome this deviation. The positive value of this interaction component indicates the solute-solute repulsion as aforementioned.

In Fig. 4, the navy short dash and green solid curves represent predictions made using the DS model. The navy short dash curve is based on a constant f^{gb} , same as the SS condition, while the green curve contains a variable f^{gb} which is a function of solute concentration obtained at 300 K. Both DS prediction curves fit better against the real \bar{X}^{gb} than those obtained by Eq. (9) without solute-solute interactions. This clearly declares the great improvement of incorporating solute-solute interactions in the DS prediction model compared to the SS model. With varying f^{gb} , the green curve can perfectly fit the real \bar{X}^{gb} , as shown in Fig. 4. However, the green curve starts to deviate from the real \bar{X}^{gb} at higher total solute concentrations, e.g. $X^{\text{tot}} \geq 8$ at.%, which can be attributed to the formation of the ordered structure in bulk regions (Fig. 2(d)). Thus, Eq. (16) can perfectly predict the GB segregation in Al-Mg with solute-solute repulsion before forming secondary phases.

6.2. Solute-solute attraction

Next, it is necessary to demonstrate segregation state in Ag-Ni, Ag-Cu, and Al-Ni where the solute-solute attraction was observed. Fig. 5(a) displays the structure and solute distribution of the Ag-Ni alloy at Ni-10 at.%, where all the Ni atoms segregate to GBs. These solute atoms concentrate at triple and quadruple junctions, and form Ni clusters as reported by previous studies [54,55]. This phenomenon suggests the strong segregation feature of Ni in Ag, which confirms the negative characteristic segregation energy in both SS and DS spectra. Furthermore, the more negative value in characteristic segregation energy of the DS spectra also verifies the clustering tendency of Ni atoms in Ag. As for the Ag-Cu system, intense segregation and clustering of Cu in Ag can also be observed, as shown in Fig. 5(b). Unlike the Ni in Ag, there is no obvious region preference of the Cu atoms in Ag. They simply tend to segregate and form clusters at GBs.

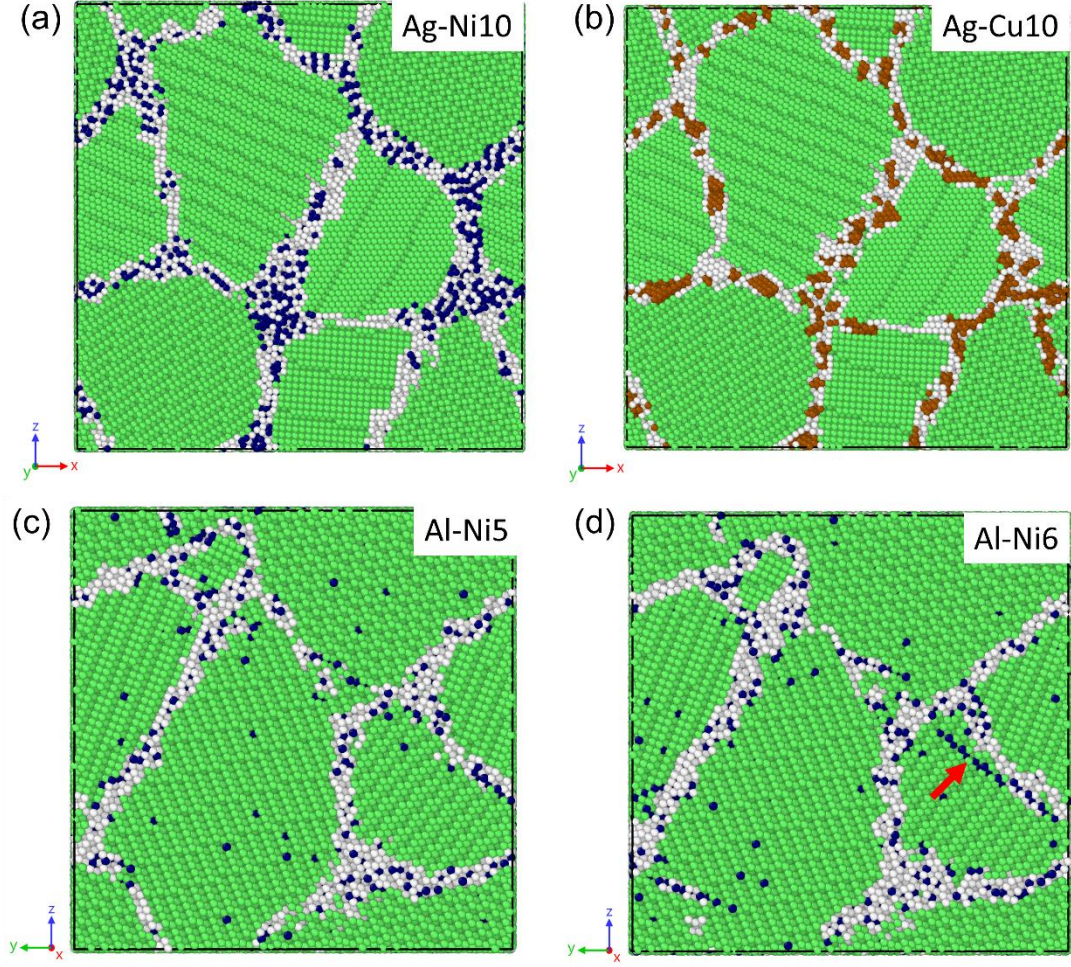


Fig. 5 The structures and solute distributions in the (a) Ag-Ni 10 at.%, (b) Ag-Cu 10 at.%, (c) Al-Ni 5 at.%, and (d) Al-Ni 6 at.% systems after hybrid MD/MC simulations at 300 K. The navy spheres are Ni atoms, while the brown ones are cooper. Green and gray spheres represent FCC and other structures, respectively. The red arrow in (d) indicates the ordered structure.

Table 2 Parameters of Ag-Ni, Ag-Cu, and Al-Ni used for the DS prediction model, i.e., Eq. (16). The α , μ , and σ are obtained by fitting the SS and DS segregation energy spectra using the skew-normal distribution.

		α	μ , kJ/mol	σ , kJ/mol	ΔE^μ , kJ/mol	ζ	$\Delta E_{\text{int}}^{\text{add}}$, kJ/mol
Ag-Ni	SS	0.41	-10.5	17.8	-10.6	5.73	-60.8
	DS	1.26	-21.1	33.2			
Ag-Cu	SS	-1	7.1	11.9	-1.6	1.28	-2.05
	DS	-0.9	5.5	16.9			
Al-Ni	SS	1.46	-2.5	24.8	-3.5	1.62	-5.65
	DS	1.7	-6	34.4			

Ni atoms also exhibit a tendency to segregate to GBs in Al, as illustrated in Fig. 5(c) where the Ni concentration is 5 at.%, although not as intensely as Ni in Ag since there are many Ni atoms left in bulk regions. However, when the Ni concentration increases to 6 at.%, ordered structures can be observed in the bulk regions of Al-Ni after the hybrid MD/MC simulations at 300 K, as shown in Fig. 5(d). Thus, we focus on the segregation prediction with the solute concentration up to 5 at.%, before forming the secondary phases.

In Table 2, the $\Delta E_{\text{int}}^{\text{add}} = -60.8$ kJ/mol in Ag-Ni indicates the extreme intense attraction among Ni atoms in Ag, which, in turn, explains the formation of Ni clusters at GBs, while no Ni atoms can be observed in bulk regions. The additional solute-solute interaction component for Ag-Cu and Al-Ni are -2.05 kJ/mol and -5.65 kJ/mol, respectively, which also enhance the solute-solute attraction feature in the two systems. These parameters were used for GB segregation prediction using Eq. (16) at 300 K.

Fig. 6 shows the comparison of the GB segregation prediction accuracy between the DS and the SS models against the resulting real \bar{X}^{gb} obtained from hybrid MD/MC simulation at 300 K. In the case of Ag-Ni, both the SS and DS models, with varying f^{gb} , can accurately predict the real \bar{X}^{gb} , as shown in Fig. 6(a). However, employing a constant f^{gb} will lead to significant deviation from the real \bar{X}^{gb} at 300 K. In particular, the behavior of DS prediction curve looks like the McLean isotherm, demonstrating a linear relationship between \bar{X}^{gb} and X^{tot} even at high solute concentrations, reaching up to 10 at.%. This phenomenon can be attributed to the extreme negative solute-solute interactions.

In Fig. 6(b) and (c), all the prediction curves are obtained with the f^{gb} as a function of X^{tot} in the corresponding system, with the relationship parameters shown in Fig. 2(b). In Ag-Cu, significant deviation from the real \bar{X}^{gb} can be observed in the prediction curve obtained by solving Eq. (9), where absolutely no solute-solute interactions are included, as shown in Fig. 6(b). When using the DS model without additional solute-solute interactions (i.e., $\Delta E_{\text{int}}^{\text{add}} = 0$ kJ/mol), the segregation prediction (represented by the blue dash curve in Fig. 6(b)) shows a remarkable improvement compared to that of the SS model. It closely approaches the real \bar{X}^{gb} with only minor deviations. Similar improvement can also be observed in Al-Ni, as shown in Fig. 6(c). This confirms that partial

solute-solute interactions are included in the DS spectra, illustrated by the improved skew-normal fitting parameters. Even though the whole picture of solute-solute interactions cannot be fully described by the DS spectra, it indeed improves the segregation prediction. Incorporating the additional solute-solute interaction component (i.e., finite $\Delta E_{\text{int}}^{\text{add}}$) in Eq. (16), the prediction curves (illustrated by the green curves in Fig. 6(b) and (c)) accurately align with the positions of the real \bar{X}^{gb} , indicating the reliability of our DS segregation framework.

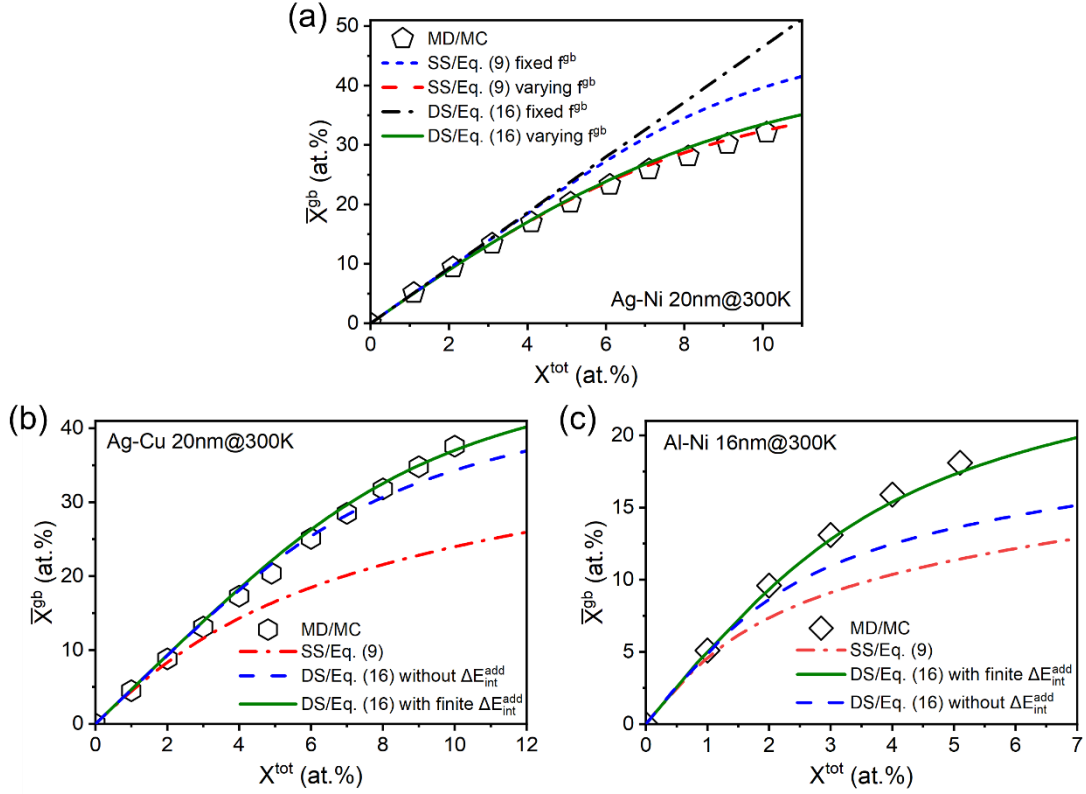


Fig. 6 GB segregation prediction using Eq. (16) at 300 K, and comparison with the SS prediction in (a) Ag-Ni, (b) Ag-Cu, and (c) Al-Ni. The real \bar{X}^{gb} obtained by hybrid MD/MC simulations at 300 K serves as the benchmark of examining the accuracy of segregation prediction models.

So far, we have introduced the DS segregation framework and explained how to use it to predict GB segregation in several binary systems. We also demonstrated a great improvement in prediction accuracy compared to the classical approach and spectral ones based on dilute conditions. In the next section, we will discuss the size and temperature effects on the prediction accuracy of the DS model, followed by discussions on limitations of this prediction model.

7. Discussions

7.1. Size effects on prediction accuracy

We conducted hybrid MD/MC simulations employing the L-NC-Al structure at 300 K to examine the potential effects of the DS model on its prediction accuracy. The edge length of this cubic NC structure is 40 nm. There are eighteen randomly oriented grains with an average grain size of 15 nm, which is two times larger than that of the NC-Al (16 nm)³ structure. The higher GB solute concentrations can be observed in the large NC model compared to those in the small structure after “real” segregation at 300 K, as shown in Fig. 7(a). This size dependence in \bar{X}^{gb} can be attributed to the relatively low GB volume fraction in the larger specimen, which can be seen from Fig. 3(a). As for the prediction accuracy, the DS model can accurately align with the real \bar{X}^{gb} at 300 K. The maximum prediction errors with respect to the hybrid MD/MC results are 4%, as shown in Fig. 7(b), indicating the outstanding prediction accuracy for different sizes using the DS model.

Grain size dependence of solute segregation has been observed by experiments with larger grain sizes resulting in higher solute concentration at GBs [72–74], due to the smaller GB area over volume ratio [72]. These findings confirm our observation that \bar{X}^{gb} shows a strong size dependence. Nevertheless, the DS model prediction curves also exhibit a size dependence and fit well with the real \bar{X}^{gb} . Tuchinda and Schuh [35] reported a strong size effect on the McLean segregation energy with a deviation of 6 kJ/mol observed upon increasing the grain size from 5 nm to 40nm. However, we used the same spectral parameters and solute-solute interaction term in both prediction processes. The prediction accuracy is reliable in both cases. This suggests that the DS model can successfully predict real segregation in those NC structures with different grain sizes. This feature of the DS prediction model benefits from the varying GB volume fractions which intrinsically incorporates the critical grain size information.

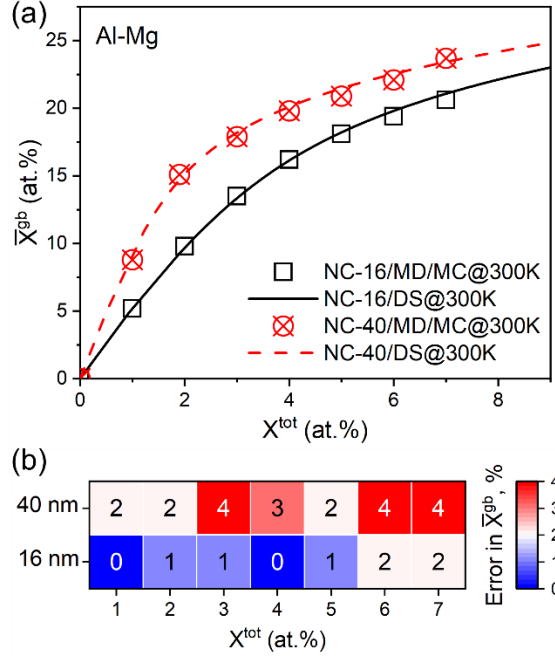


Fig. 7 (a) GB segregation prediction using Eq. (16) for the Al-Mg system with different sizes against the real \bar{X}^{gb} obtained from hybrid MD/MC simulations at 300 K. (b) The corresponding DS prediction errors in \bar{X}^{gb} at each total solute concentration.

7.2. Temperature effects on prediction accuracy

Temperature is another important factor that affects solute segregation at GBs. Previous studies reported that the chemical composition at GBs strongly depends on the annealing temperatures, which can be attributed to the differences in segregation enthalpies [75,76] and segregation free energies [77]. This temperature dependence of solute segregation was also confirmed by hybrid MC/MS simulations [43]. To find out if temperature affects the DS prediction accuracy, we conducted hybrid MD/MC simulations at different temperatures in Al-Mg. Indeed, the real \bar{X}^{gb} demonstrates a notable temperature dependence with higher temperatures leading to lower GB solute concentrations at the same total solute concentration, as shown in Fig. 8(a). The temperature dependency becomes evident when the total solute concentration exceeds 1 at.%, which represents the dilute limit (shown in Fig. 4) of the Al-Mg system. At higher total solute concentrations, there is a larger discrepancy in GB solute concentration between different temperatures.

The DS prediction accuracy in \bar{X}^{gb} without correction in ΔE_{int}^{add} at different temperatures is shown in Supplementary Fig. 1(a). Here, the maximum error of ~6% can be observed at 500 K, while the

maximum error is only around 5% when the temperature is 400 K. Such a high level of prediction accuracy is acceptable in engineering applications, indicating the reliability of the DS segregation prediction at different temperatures. However, the maximum prediction error increases with temperature from 2% at 300 K to 6% at 500 K. Two potential problems may be responsible for this increase in maximum error: (i) the artificial nature of the temperature dependence in Eq. (16), because all the parameters used here are obtained from the 0 K segregation energy spectra, where entropic contributions were ignored [37]; (ii) the fixed solute-solute interaction component instead of a temperature-dependent term [78]. To solve the problem (i), large amounts of extra atomistic simulations [37,79] will be needed to obtain the entropic contributions.

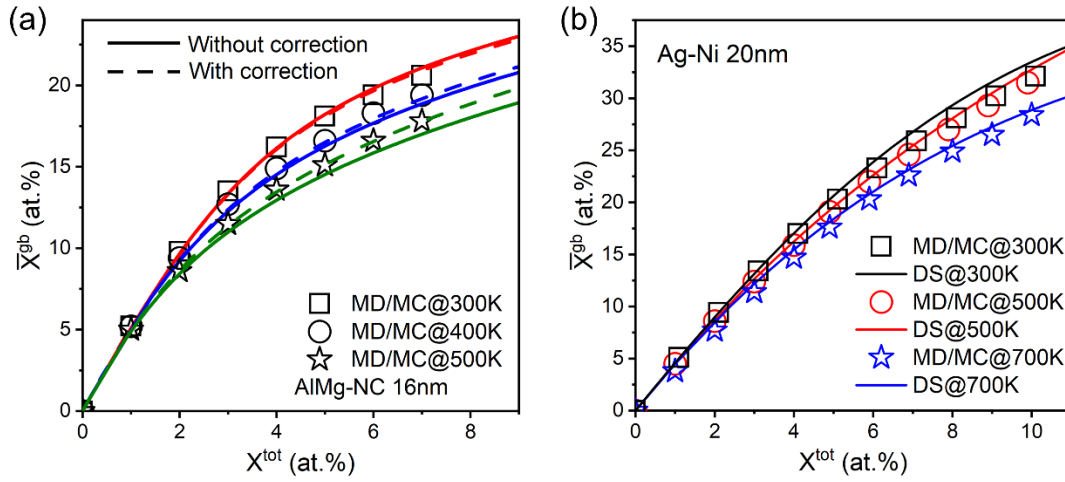


Fig. 8 (a) Comparison of GB segregation prediction using the DS model between the without and with correction in ΔE_{int}^{add} in Al-Mg at different temperatures. (b) GB segregation prediction using the DS model without correction in ΔE_{int}^{add} in Ag-Ni at different temperatures.

Nevertheless, to solve problem (ii), we can simply assume that the additional solute-solute interactions are linearly related to temperature by ignoring the temperature-induced variation in distance [78]. Then, we can manually find out the “best” fitted (i.e., near zero prediction error) ΔE_{int}^{add} equal to 6.53 kJ/mol, 5.65 kJ/mol, and 4.64 kJ/mol for 300 K, 400 K, and 500 K conditions, respectively. Thereafter, the correlation between ΔE_{int}^{add} and temperature T can be obtained: $\Delta E_{int}^{add} = 8.38667 - 0.00645T$. So, we can obtain the corrected additional solute-solute interactions $\Delta E_{int,c}^{add}$ are about 6.45 kJ/mol, 5.81 kJ/mol, and 5.16 kJ/mol for 300 K, 400 K, and 500 K conditions, respectively. In the following steps, we can use these corrected additional solute-solute interactions

for predictions. The GB segregation prediction (dashed) curves with correction in $\Delta E_{\text{int}}^{\text{add}}$ fit better compared to the original (solid) ones, as shown in Fig. 8(a). Moreover, the higher temperature will result in a greater improvement in prediction accuracy. This trend can also be confirmed by the prediction errors in \bar{X}^{gb} with the maximum error of no more than 2%, as shown in Supplementary Fig. 1(b). This improvement in prediction accuracy explains that there is indeed a temperature dependence in solute-solute interactions. Thus, the increasing prediction errors at elevated temperatures can be overcome by the linear simplification in the temperature dependence of solute-solute interactions.

Furthermore, the high accuracy of the DS predictions can also be observed in the Ag-Ni at different temperatures with only negligible deviation from the hybrid MD/MC results, even without any correction in $\Delta E_{\text{int}}^{\text{add}}$, as shown in Fig. 8(b). This indicates that the solute-solute interactions in Ag-Ni are not significantly affected by temperature, as supported by the snapshots showing that the solutes always segregate as clusters at GBs regardless of temperature (Supplementary Fig. 2). It further confirms the applicability of the DS model in different binary systems with a wide range of temperatures.

7.3. Limitations of the DS model

Although we have shown that the DS model can accurately predict GB segregation in several binary systems, there are still two limitations: (i) the GB volume fraction is an empirical function depending on the alloy systems or potentials; (ii) it cannot be used to predict the GB segregation after forming secondary phases when the total solute concentration exceeds a critical value.

With the fixed f^{gb} , it is impossible to correctly predict the GB segregation due to the total solute concentration dependence of GB volume fraction [51], as shown in Fig. 3(a). In this work, we use three parameters m , n , and r to describe the total solute concentration dependence of the GB volume fraction. However, these three parameters are obtained from the hybrid MD/MC simulations. Moreover, the GB volume fraction is also a function of grain sizes [11], as shown in Fig. 3(a). Thus, more work is necessary to construct a function or a database to describe the total solute concentration dependence of the GB volume fraction that can cover all the possible binaries.

Once secondary phases being formed in the polycrystals, it is difficult to predict the distribution of solute atoms, which can significantly influence the solute concentration at GBs. For example, ordered structures can be observed in Al-Mg and Al-Ni after hybrid MD/MC simulations when the total solute concentration is greater than 8 at.% and 6 at.%, respectively. However, the solute atoms were swapped back to bulk regions to form the ordered structures other than segregation at GBs. Therefore, the GB thickness was greatly reduced, as shown in Fig. 2(d). This uncertainty increases the deviation of GB segregation prediction. Thus, Eq. (16) is only applicable when the total solute concentration is lower than the critical one when forming secondary phases.

7.4. Comparison with other spectral approaches

Previously, we have introduced two other spectral models to predict GB segregation with consideration of solute-solute interactions when the solute concentration is beyond dilute limit [43,44]. Both approaches use the SS segregation energy spectrum where the solute-solute interactions are absent. Moreover, hybrid MC/MS simulations were considered as the true segregation where GBs were treated as static at 0 K. Thus, the GB volume fraction was treated as a constant in their studies. One of them relies on fitting the hybrid MC/MS data as the solute-solute interaction term [43]. The other one computed the solute-solute interactions by atomistic simulations, where the value is physically informed, but it is computationally expensive. Both studies have shown considerable prediction accuracy against the hybrid MC/MS results.

In this work, the DS segregation energy spectra inherently incorporate the solute-solute interactions. By combining the varying GB volume fraction with the additional solute-solute interaction term, the DS model can be used to predict the GB segregation with considerable accuracy against the hybrid MD/MC simulations, where the GBs exhibit dynamic behaviors at finite temperatures. For instance, the formation of secondary phases was observed during the hybrid MD/MC simulations in Al-Mg and Al-Ni, and the thickening behavior of GBs after segregation. However, no secondary phases were reported in the two spectral approaches [43,44], likely due to the static nature of the hybrid MC/MS simulations. Furthermore, compared to the atomistic approach [44], the DS model requires fewer computing resources.

In addition, Tuchinda and Schuh [37] linearly related the vibrational entropy to the per-site segregation energy, which can effectively describe the temperature dependence of solute segregation. However extra harmonic simulations are needed to determine the vibrational contribution. Menon et al. [79] employed the thermodynamic integration method to determine the per-site segregation free energy, which inherently contains the temperature effects. However, no solute-solute interaction term was defined in both studies. In this work, we observe that the temperature effects on prediction accuracy using the DS model are negligible with only acceptable disagreement between the predictions and hybrid MD/MC results. Moreover, we have shown that it is possible to overcome the increased prediction errors using the linear correction of the additional solute-solute interactions.

8. Conclusion

The main conclusions of this work can be drawn as follows:

- (1) We proposed the DS segregation framework which was used to calculate the solute segregation energy spectrum in several binary systems, e.g., Al-Mg, Al-Ni, Ag-Ni, and Ag-Cu. The DS spectrum is different from the SS spectrum with wider energy range but lower peak probability density in each system. The skew-normal fitting characteristic segregation energy of the SS and DS spectra can be considered as the indicator of repulsive or attractive solute-solute interactions. The larger μ_{DS} than μ_{SS} represents the solute-solute repulsion, e.g., Al-Mg, while the smaller μ_{DS} than μ_{SS} indicates the attractive solute-solute interactions, e.g., Al-Ni, Ag-Ni, and Ag-Cu.
- (2) The hybrid MD/MC simulation results serve as the real segregation state at finite temperatures. At higher total solute concentrations, ordered structures were observed in Al-Mg and Al-Ni, which are consistent with previous studies. The polycrystal structures after hybrid MD/MC simulations confirm the GB thickening behavior with solute segregation at GBs. Thus, the varying GB volume fraction is needed for further analysis.
- (3) Combining with the additional solute-solute interaction term and varying GB volume fraction, we have shown that the DS model can be successfully used to predict the GB segregation in several binary systems with either solute-solute repulsion (e.g., Al-Mg) or solute-solute attraction (e.g., Al-Ni, Ag-Ni, and Ag-Cu).

- (4) The size effect on GB segregation prediction of the DS model was assessed in the Al-Mg system. The results show that the DS model can accurately predict the segregation behavior in a larger NC structure using the parameters from a smaller one. This indicates that it can be successfully used to predict the GB segregation with different grain sizes since the GB volume fraction intrinsically contains the grain size information. It further confirms the necessity of the varying GB volume fraction.
- (5) An increase in prediction error was observed at elevating temperatures in Al-Mg using the DS model, even though the maximum error was only 6%. This can be attributed to the temperature dependence of solute-solute interactions which can be overcome by linear simplification of the additional solute-solute interaction term.

In summary, the DS segregation is a reliable model to predict the GB segregation behaviors in various binary systems. The prediction accuracy is independent of grain sizes. Nevertheless, future work is still needed to explore the dependencies of GB volume fraction on temperatures, grain sizes, and total solute concentrations. This study provides a novel method to predict solute segregation at GBs at finite temperatures with significant accuracy.

Acknowledgement

This research was supported by the NSERC Discovery Grant (RGPIN-2019-05834), Canada, and the use of computing resources provided by the Digital Research Alliance of Canada. During the preparation of this manuscript, the authors used ChatGPT to improve its readability. After using this tool, the authors reviewed and edited the manuscript as needed and take full responsibility for the content of the publication.

Declaration of competing interest

The authors declare that they have no known competing financial interests or personal relationships that could influence the work reported in this paper.

Reference

- [1] J.R. Weertman, Hall-Petch strengthening in nanocrystalline metals, *Materials Science and Engineering: A* 166 (1993) 161–167. [https://doi.org/10.1016/0921-5093\(93\)90319-A](https://doi.org/10.1016/0921-5093(93)90319-A).
- [2] N. Hansen, Hall–Petch relation and boundary strengthening, *Scripta Materialia* 51 (2004) 801–806. <https://doi.org/10.1016/j.scriptamat.2004.06.002>.
- [3] Z.C. Cordero, B.E. Knight, C.A. Schuh, Six decades of the Hall–Petch effect – a survey of grain-size strengthening studies on pure metals, *International Materials Reviews* 61 (2016) 495–512. <https://doi.org/10.1080/09506608.2016.1191808>.
- [4] H. Natter, M. Schmelzer, R. Hempelmann, Nanocrystalline nickel and nickel-copper alloys: Synthesis, characterization, and thermal stability, *Journal of Materials Research* 13 (1998) 1186–1197.
- [5] K.A. Darling, B.K. VanLeeuwen, C.C. Koch, R.O. Scattergood, Thermal stability of nanocrystalline Fe–Zr alloys, *Materials Science and Engineering: A* 527 (2010) 3572–3580. <https://doi.org/10.1016/j.msea.2010.02.043>.
- [6] V.Y. Gertsman, R. Birringer, On the room-temperature grain growth in nanocrystalline copper, *Scripta Metallurgica et Materialia* 30 (1994) 577–581.
- [7] M. Ames, J. Markmann, R. Karos, A. Michels, A. Tschöpe, R. Birringer, Unraveling the nature of room temperature grain growth in nanocrystalline materials, *Acta Materialia* 56 (2008) 4255–4266. <https://doi.org/10.1016/j.actamat.2008.04.051>.
- [8] R. Kirchheim, Grain coarsening inhibited by solute segregation, *Acta Materialia* 50 (2002) 413–419. [https://doi.org/10.1016/S1359-6454\(01\)00338-X](https://doi.org/10.1016/S1359-6454(01)00338-X).
- [9] D.L. Beke, C. Cserhádi, I.A. Szabó, Segregation inhibited grain coarsening in nanocrystalline alloys, *Journal of Applied Physics* 95 (2004) 4996–5001. <https://doi.org/10.1063/1.1688461>.
- [10] A. Detor, C. Schuh, Grain boundary segregation, chemical ordering and stability of nanocrystalline alloys: Atomistic computer simulations in the Ni–W system, *Acta Materialia* 55 (2007) 4221–4232. <https://doi.org/10.1016/j.actamat.2007.03.024>.
- [11] J.R. Trelewicz, C.A. Schuh, Grain boundary segregation and thermodynamically stable binary nanocrystalline alloys, *Phys. Rev. B* 79 (2009) 094112. <https://doi.org/10.1103/PhysRevB.79.094112>.
- [12] H.A. Murdoch, C.A. Schuh, Estimation of grain boundary segregation enthalpy and its role in stable nanocrystalline alloy design, *J. Mater. Res.* 28 (2013) 2154–2163. <https://doi.org/10.1557/jmr.2013.211>.
- [13] T. Chookajorn, H.A. Murdoch, C.A. Schuh, Design of Stable Nanocrystalline Alloys, *Science* 337 (2012) 951–954. <https://doi.org/10.1126/science.1224737>.
- [14] J.F. Nie, Y.M. Zhu, J.Z. Liu, X.Y. Fang, Periodic Segregation of Solute Atoms in Fully Coherent Twin Boundaries, *Science* 340 (2013) 957–960. <https://doi.org/10.1126/science.1229369>.
- [15] D. McLean, *Grain Boundaries in Metals*, [M] Oxford, Clarendon Press, 1957.
- [16] R.H. (Ralph H. Fowler, E.A. (Edward A. Guggenheim, *Statistical thermodynamics : a version of statistical mechanics for students of physics and chemistry*, Cambridge University Press, 1956. <https://cir.nii.ac.jp/crid/1130282268789803648>.
- [17] P. Lejcek, *Grain Boundary Segregation in Metals*, Springer Berlin Heidelberg, Berlin, Heidelberg, 2010. <https://doi.org/10.1007/978-3-642-12505-8>.

- [18]P. Lejcek, S. Hofmann, Thermodynamic state functions of interfacial segregation and their role in the compensation effect, *Rev. Adv. Mater. Sci* 21 (2009) 27.
- [19]M. Wagih, Y. Naunheim, T. Lei, C.A. Schuh, Grain boundary segregation predicted by quantum-accurate segregation spectra but not by classical models, *Acta Materialia* 266 (2024) 119674. <https://doi.org/10.1016/j.actamat.2024.119674>.
- [20]E.D. Hondros, M.P. Seah, The theory of grain boundary segregation in terms of surface adsorption analogues, *Metall Trans A* 8 (1977) 1363–1371. <https://doi.org/10.1007/BF02642850>.
- [21]A.R. Miedema, Simple model for alloys, *Philips Tech. Rev* 33 (1973) 149–160.
- [22]F.R. De Boer, W. Mattens, R. Boom, A.R. Miedema, A.K. Niessen, *Cohesion in metals. Transition metal alloys*, (1988).
- [23]H. Bakker, Enthalpies in alloys, Miedema's semi-empirical model, *Trans. Tech. Publications* (1998).
- [24]S. Pal, K.V. Reddy, T. Yu, J. Xiao, C. Deng, The spectrum of atomic excess free volume in grain boundaries, *J Mater Sci* 56 (2021) 11511–11528. <https://doi.org/10.1007/s10853-021-06028-4>.
- [25]D.N. Seidman, Subnanoscale Studies of Segregation at Grain Boundaries: Simulations and Experiments, *Annu. Rev. Mater. Res.* 32 (2002) 235–269. <https://doi.org/10.1146/annurev.matsci.32.011602.095455>.
- [26]T. Nenninger, F. Sansoz, Local atomic environment analysis of short and long-range solute-solute interactions in a symmetric tilt grain boundary, *Scripta Materialia* 222 (2023) 115045. <https://doi.org/10.1016/j.scriptamat.2022.115045>.
- [27]F. Sansoz, X. Ke, Hall–Petch strengthening limit through partially active segregation in nanocrystalline Ag-Cu alloys, *Acta Materialia* 225 (2022) 117560. <https://doi.org/10.1016/j.actamat.2021.117560>.
- [28]C.L. White, W.A. Coghlan, The spectrum of binding energies approach to grain boundary segregation, *MTA* 8 (1977) 1403–1412. <https://doi.org/10.1007/BF02642853>.
- [29]C.L. White, D.F. Stein, Sulfur segregation to grain boundaries in Ni 3 Al and Ni 3 (Al, Ti) alloys, *Metallurgical Transactions A* 9 (1978) 13–22.
- [30]T. Mütschele, R. Kirchheim, Segregation and diffusion of hydrogen in grain boundaries of palladium, *Scripta Metallurgica* 21 (1987) 135–140.
- [31]R. Kirchheim, Hydrogen solubility and diffusivity in defective and amorphous metals, *Progress in Materials Science* 32 (1988) 261–325.
- [32]M. Wagih, C.A. Schuh, Spectrum of grain boundary segregation energies in a polycrystal, *Acta Materialia* 181 (2019) 228–237. <https://doi.org/10.1016/j.actamat.2019.09.034>.
- [33]M. Wagih, P.M. Larsen, C.A. Schuh, Learning grain boundary segregation energy spectra in polycrystals, *Nat Commun* 11 (2020) 6376. <https://doi.org/10.1038/s41467-020-20083-6>.
- [34]M. Wagih, C.A. Schuh, Learning Grain-Boundary Segregation: From First Principles to Polycrystals, *Phys. Rev. Lett.* 129 (2022) 046102. <https://doi.org/10.1103/PhysRevLett.129.046102>.
- [35]N. Tuchinda, C.A. Schuh, Grain size dependencies of intergranular solute segregation in nanocrystalline materials, *Acta Materialia* 226 (2022) 117614. <https://doi.org/10.1016/j.actamat.2021.117614>.
- [36]N. Tuchinda, C.A. Schuh, Triple junction solute segregation in Al-based polycrystals, *Phys. Rev. Materials* 7 (2023) 023601. <https://doi.org/10.1103/PhysRevMaterials.7.023601>.
- [37]N. Tuchinda, C.A. Schuh, The vibrational entropy spectra of grain boundary segregation in

- polycrystals, *Acta Materialia* 245 (2023) 118630. <https://doi.org/10.1016/j.actamat.2022.118630>.
- [38] Z. Zhang, C. Deng, Hydrostatic pressure-induced transition in grain boundary segregation tendency in nanocrystalline metals, *Scripta Materialia* 234 (2023) 115576. <https://doi.org/10.1016/j.scriptamat.2023.115576>.
- [39] T.P. Matson, C.A. Schuh, Phase and defect diagrams based on spectral grain boundary segregation: A regular solution approach, *Acta Materialia* 265 (2024) 119584. <https://doi.org/10.1016/j.actamat.2023.119584>.
- [40] D. Scheiber, L. Romaner, R. Pippan, P. Puschnig, Impact of solute-solute interactions on grain boundary segregation and cohesion in molybdenum, *Phys. Rev. Materials* 2 (2018) 093609. <https://doi.org/10.1103/PhysRevMaterials.2.093609>.
- [41] Z. Huang, J.-F. Nie, Solute-solute interactions and their impacts on solute co-segregation and interfacial cohesion of $\{10\bar{1}2\}$ twin boundary in zinc, *Journal of Materials Science & Technology* 138 (2023) 117–128. <https://doi.org/10.1016/j.jmst.2022.07.051>.
- [42] W. Xing, A.R. Kalidindi, D. Amram, C.A. Schuh, Solute interaction effects on grain boundary segregation in ternary alloys, *Acta Materialia* 161 (2018) 285–294. <https://doi.org/10.1016/j.actamat.2018.09.005>.
- [43] M. Wagih, C.A. Schuh, Grain boundary segregation beyond the dilute limit: Separating the two contributions of site spectrality and solute interactions, *Acta Materialia* 199 (2020) 63–72. <https://doi.org/10.1016/j.actamat.2020.08.022>.
- [44] T.P. Matson, C.A. Schuh, Atomistic Assessment of Solute-Solute Interactions during Grain Boundary Segregation, *Nanomaterials* 11 (2021) 2360. <https://doi.org/10.3390/nano11092360>.
- [45] D.A. Steigerwald, P. Wynblatt, Calculation of the anisotropy of equilibrium surface composition in metallic solid solutions using the embedded atom method, *Surface Science* 193 (1988) 287–303.
- [46] J. Creuze, F. Berthier, R. Tétot, B. Legrand, G. Tréglia, Intergranular segregation and vibrational effects: A local analysis, *Phys. Rev. B* 61 (2000) 14470–14480. <https://doi.org/10.1103/PhysRevB.61.14470>.
- [47] P. Lejček, L. Zheng, S. Hofmann, M. Šob, Applied Thermodynamics: Grain Boundary Segregation, *Entropy* 16 (2014) 1462–1483. <https://doi.org/10.3390/e16031462>.
- [48] M. Parrinello, A. Rahman, Polymorphic transitions in single crystals: A new molecular dynamics method, *Journal of Applied Physics* 52 (1981) 7182–7190. <https://doi.org/10.1063/1.328693>.
- [49] K. Ishida, Effect of grain size on grain boundary segregation, *Journal of Alloys and Compounds* 235 (1996) 244–249. [https://doi.org/10.1016/0925-8388\(95\)02094-2](https://doi.org/10.1016/0925-8388(95)02094-2).
- [50] S.G. Kim, Y.B. Park, Grain boundary segregation, solute drag and abnormal grain growth, *Acta Materialia* 56 (2008) 3739–3753. <https://doi.org/10.1016/j.actamat.2008.04.007>.
- [51] C. Chen, Y. Chen, J. Yu, M. Liu, J. Zhang, Microstructural evolution and multi-mechanism strengthening model of nanocrystalline Al-Mg alloys, *Journal of Alloys and Compounds* 983 (2024) 173905. <https://doi.org/10.1016/j.jallcom.2024.173905>.
- [52] M.R. Chellali, Z. Balogh, H. Bouchikhaoui, R. Schlesiger, P. Stender, L. Zheng, G. Schmitz, Triple Junction Transport and the Impact of Grain Boundary Width in Nanocrystalline Cu, *Nano Lett.* 12 (2012) 3448–3454. <https://doi.org/10.1021/nl300751q>.
- [53] R.K. Koju, Y. Mishin, Relationship between grain boundary segregation and grain boundary diffusion in Cu-Ag alloys, *Phys. Rev. Materials* 4 (2020) 073403. <https://doi.org/10.1103/PhysRevMaterials.4.073403>.

- [54] E.-A. Picard, F. Sansoz, Ni solute segregation and associated plastic deformation mechanisms into random FCC Ag, BCC Nb and HCP Zr polycrystals, *Acta Materialia* 240 (2022) 118367. <https://doi.org/10.1016/j.actamat.2022.118367>.
- [55] Z. Pan, F. Sansoz, Heterogeneous solute segregation suppresses strain localization in nanocrystalline Ag-Ni alloys, *Acta Materialia* 200 (2020) 91–100. <https://doi.org/10.1016/j.actamat.2020.08.074>.
- [56] Z. Zhang, C. Deng, Solid solution softening in single crystalline metal nanowires studied by atomistic simulations, *Phys. Rev. Materials* 7 (2023) 053611. <https://doi.org/10.1103/PhysRevMaterials.7.053611>.
- [57] M. Wagih, C.A. Schuh, Viewpoint: Can symmetric tilt grain boundaries represent polycrystals?, *Scripta Materialia* 237 (2023) 115716. <https://doi.org/10.1016/j.scriptamat.2023.115716>.
- [58] S. Plimpton, Fast Parallel Algorithms for Short-Range Molecular Dynamics, *Journal of Computational Physics* 117 (1995) 1–19. <https://doi.org/10.1006/jcph.1995.1039>.
- [59] A. Stukowski, Visualization and analysis of atomistic simulation data with OVITO—the Open Visualization Tool, *Modelling Simul. Mater. Sci. Eng.* 18 (2009) 015012. <https://doi.org/10.1088/0965-0393/18/1/015012>.
- [60] P.M. Larsen, S. Schmidt, J. Schiøtz, Robust structural identification via polyhedral template matching, *Modelling and Simulation in Materials Science and Engineering* 24 (2016) 055007.
- [61] M.S. Daw, M.I. Baskes, Embedded-atom method: Derivation and application to impurities, surfaces, and other defects in metals, *Phys. Rev. B* 29 (1984) 6443–6453. <https://doi.org/10.1103/PhysRevB.29.6443>.
- [62] M.I. Mendelev, M. Asta, M.J. Rahman, J.J. Hoyt, Development of interatomic potentials appropriate for simulation of solid–liquid interface properties in Al–Mg alloys, *Philosophical Magazine* 89 (2009) 3269–3285. <https://doi.org/10.1080/14786430903260727>.
- [63] Z. Pan, V. Borovikov, M.I. Mendelev, F. Sansoz, Development of a semi-empirical potential for simulation of Ni solute segregation into grain boundaries in Ag, *Modelling Simul. Mater. Sci. Eng.* 26 (2018) 075004. <https://doi.org/10.1088/1361-651X/aadea3>.
- [64] P.L. Williams, Y. Mishin, J.C. Hamilton, An embedded-atom potential for the Cu–Ag system, *Modelling Simul. Mater. Sci. Eng.* 14 (2006) 817–833. <https://doi.org/10.1088/0965-0393/14/5/002>.
- [65] G.P. Purja Pun, Y. Mishin, Development of an interatomic potential for the Ni–Al system, *Philosophical Magazine* 89 (2009) 3245–3267. <https://doi.org/10.1080/14786430903258184>.
- [66] B. Sadigh, P. Erhart, A. Stukowski, A. Caro, E. Martinez, L. Zepeda-Ruiz, Scalable parallel Monte Carlo algorithm for atomistic simulations of precipitation in alloys, *Phys. Rev. B* 85 (2012) 184203. <https://doi.org/10.1103/PhysRevB.85.184203>.
- [67] P. Hirel, AtomsK: A tool for manipulating and converting atomic data files, *Computer Physics Communications* 197 (2015) 212–219. <https://doi.org/10.1016/j.cpc.2015.07.012>.
- [68] G. Itoh, B. Cottreau, M. Kanno, Precipitation of the intermediate phase β' in an Al-8% Mg alloy, *Materials Transactions, JIM* 31 (1990) 1041–1049.
- [69] M. Boucheur, D. Hamana, T. Laoui, GP zones and precipitate morphology in aged Al–Mg alloys, *Philosophical Magazine A* 73 (1996) 1733–1740. <https://doi.org/10.1080/01418619608243010>.
- [70] X.-Y. Liu, J.B. Adams, Grain-boundary segregation in Al–10%Mg alloys at hot working temperatures, *Acta Materialia* 46 (1998) 3467–3476. [https://doi.org/10.1016/S1359-6454\(98\)00038-X](https://doi.org/10.1016/S1359-6454(98)00038-X).

- [71] A. Devaraj, W. Wang, R. Vemuri, L. Kovarik, X. Jiang, M. Bowden, J.R. Trelewicz, S. Mathaudhu, A. Rohatgi, Grain boundary segregation and intermetallic precipitation in coarsening resistant nanocrystalline aluminum alloys, *Acta Materialia* 165 (2019) 698–708. <https://doi.org/10.1016/j.actamat.2018.09.038>.
- [72] C.D. TERWILLIGER and YET-MING CHIANG, SIZE-DEPENDENT SOLUTE SEGREGATION AND TOTAL SOLUBILITY IN ULTRAFINE POLYCRYSTALS: Ca IN TiO₂, (n.d.).
- [73] K. Ishida, Effect of grain size on grain boundary segregation, *Journal of Alloys and Compounds* 235 (1996) 244–249. [https://doi.org/10.1016/0925-8388\(95\)02094-2](https://doi.org/10.1016/0925-8388(95)02094-2).
- [74] M. Aoki, Y. Chiang, I. Kosacki, L.J. Lee, H. Tuller, Y. Liu, Solute Segregation and Grain-Boundary Impedance in High-Purity Stabilized Zirconia, *Journal of the American Ceramic Society* 79 (1996) 1169–1180. <https://doi.org/10.1111/j.1151-2916.1996.tb08569.x>.
- [75] P. Lejček, J. Adimek, Anisotropy of grain boundary segregation in $Z = 5$ bicrystals of α -iron, (n.d.).
- [76] P. Lejček, S. Hofmann, Segregation enthalpies of phosphorus, carbon and silicon at $\{013\}$ and $\{012\}$ symmetrical tilt grain boundaries in an Fe-3.5 at.% Si alloy, *Acta Metallurgica et Materialia* 39 (1991) 2469–2476. [https://doi.org/10.1016/0956-7151\(91\)90026-W](https://doi.org/10.1016/0956-7151(91)90026-W).
- [77] D. Scheiber, M.N. Popov, L. Romaner, Temperature dependence of solute segregation energies at W GBs from first principles, *Scripta Materialia* 222 (2023) 115059. <https://doi.org/10.1016/j.scriptamat.2022.115059>.
- [78] H. Wennerström, J. Daicic, B.W. Ninham, Temperature dependence of atom-atom interactions, *Phys. Rev. A* 60 (1999) 2581–2584. <https://doi.org/10.1103/PhysRevA.60.2581>.
- [79] V. Menon, S. Das, V. Gavini, L. Qi, Atomistic simulations and machine learning of solute grain boundary segregation in Mg alloys at finite temperatures, *Acta Materialia* 264 (2024) 119515. <https://doi.org/10.1016/j.actamat.2023.119515>.

Supplementary materials for

Grain boundary segregation prediction with a dual-solute model

Zuoyong Zhang and Chuang Deng*

Department of Mechanical Engineering, University of Manitoba, Winnipeg, Canada MB R3T 5V6

* Corresponding author: Chuang.Deng@umanitoba.ca

Supplementary Table 1 Hybrid Molecular Dynamics/Monte Carlo (MD/MC) parameters for the Al-Mg system with $\kappa = 1000$ were obtained by test runs at 300 K. c_0 indicates the desired solute concentration, while $\Delta\mu_0$ is the chemical potential difference between the solvent and solute species. The X^{tot} and \bar{X}^{gb} are the total solute concentration and grain boundary (GB) solute concentration after hybrid MD/MC simulations, respectively. The colored region in the table below indicates the total solute concentrations that secondary phases can be observed after the hybrid MD/MC simulations.

$c_0 \times 100$, at. %	1	2	3	4	5	6	7	8	10
$\Delta\mu_0$	-1.683	-1.759	-1.847	-1.811	-1.860	-1.877	-1.885	-1.891	-1.890
X^{tot} , at. %	1	2	3	4	5	6	7	8	10
\bar{X}^{gb} , at. %	5.2	9.8	13.5	16.2	18.1	19.4	20.6	21.2	22.4

Supplementary Table 2 Hybrid MD/MC parameters for the Al-Ni system with $\kappa = 1000$ were obtained by test runs at 300 K. The X^{tot} and \bar{X}^{gb} are the total solute concentration and GB solute concentration after hybrid MD/MC simulations, respectively. The colored region in the table below indicates the total solute concentrations that secondary phases can be observed after the hybrid MD/MC simulations.

$c_0 \times 100$, at. %	1	2	3	4	5	6	7
$\Delta\mu_0$	2.261	2.189	2.156	2.081	2.053	2.051	2.045
X^{tot} , at. %	1	2	3	4	5.1	6.1	7.1
\bar{X}^{gb} , at. %	5.1	9.6	13.1	15.9	18.1	20	22.2

Supplementary Table 3 Hybrid MD/MC parameters for the Ag-Ni system with $\kappa = 1000$ were obtained by test runs at 300 K. The X^{tot} and \bar{X}^{gb} are the total solute concentration and GB solute concentration after hybrid MD/MC simulations, respectively.

$c_0 \times 100$, at. %	1	2	3	4	5	6	7	8	9	10
$\Delta\mu_0$	1.078	1.083	1.089	1.093	1.106	1.109	1.113	1.115	1.119	1.121
X^{tot} , at. %	1.1	2.1	3.1	4.1	5.1	6.1	7.1	8.1	9.1	10.1
\bar{X}^{gb} , at. %	5.1	9.4	13.4	17	20.3	23.3	25.9	28.1	30.2	32.1

Supplementary Table 4 Hybrid MD/MC parameters for the Ag-Cu system with $\kappa = 1000$ were obtained by test runs at 300 K. The X^{tot} and \bar{X}^{gb} are the total solute concentration and GB solute concentration after hybrid MD/MC simulations, respectively.

$c_0 \times 100$, at. %	1	2	3	4	5	6	7	8	9	10
$\Delta\mu_0$	0.726	0.711	0.702	0.693	0.679	0.668	0.661	0.652	0.639	0.631
X^{tot} , at. %	1	2	3	4	4.9	6	7	8	9	10
\bar{X}^{gb} , at. %	4.5	8.8	13.1	17.3	20.4	25.1	28.5	31.8	34.8	37.6

Supplementary Table 5 Hybrid MD/MC parameters for the Al-Mg system with $\kappa = 1000$ were obtained by test runs at 400 K. The X^{tot} and \bar{X}^{gb} are the total solute concentration and GB solute concentration after hybrid MD/MC simulations, respectively.

$c_0 \times 100$, at. %	1	2	3	4	5	6	7
$\Delta\mu_0$	-1.703	-1.756	-1.795	-1.825	-1.837	-1.851	-1.859
X^{tot} , at. %	1	2	3	4	5	6	7
\bar{X}^{gb} , at. %	5.2	9.4	12.7	14.9	16.6	18.3	19.4

Supplementary Table 6 Hybrid MD/MC parameters for the Al-Mg system with $\kappa = 1000$ were obtained by test runs at 500 K. The X^{tot} and \bar{X}^{gb} are the total solute concentration and GB solute concentration after hybrid MD/MC simulations, respectively.

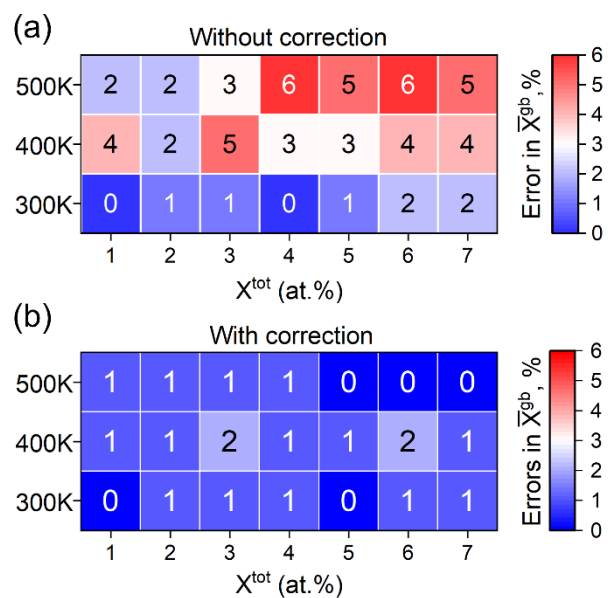
$c_0 \times 100$, at. %	1	2	3	4	5	6	7
$\Delta\mu_0$	-1.715	-1.749	-1.775	-1.792	-1.801	-1.827	-1.837
X^{tot} , at. %	1	2	3	4	5	6	7
\bar{X}^{gb} , at. %	5.0	8.6	11.5	13.6	15.1	16.6	17.8

Supplementary Table 7 Hybrid MD/MC parameters for the Ag-Ni system with $\kappa = 1000$ were obtained by test runs at 500 K. The X^{tot} and \bar{X}^{gb} are the total solute concentration and GB solute concentration after hybrid MD/MC simulations, respectively.

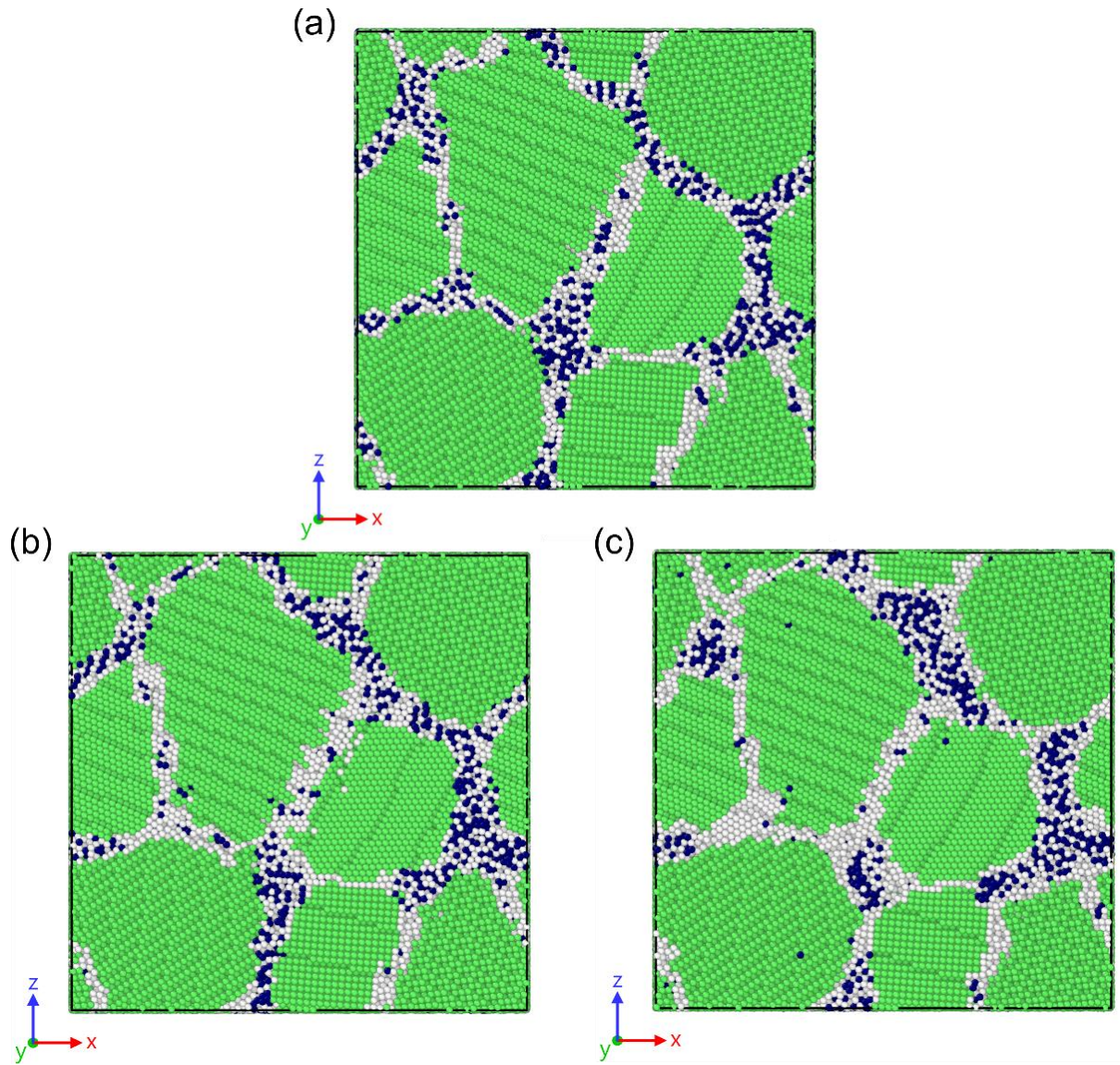
$c_0 \times 100$, at. %	1	2	3	4	5	6	7	8	9	10
$\Delta\mu_0$	1.229	1.283	1.301	1.315	1.319	1.327	1.338	1.349	1.357	1.378
X^{tot} , at. %	1	2	3	4	4.9	5.9	6.9	7.9	8.9	9.9
\bar{X}^{gb} , at. %	4.5	8.6	12.4	15.9	19.1	22.0	24.6	27.0	29.3	31.5

Supplementary Table 8 Hybrid MD/MC parameters for the Ag-Ni system with $\kappa = 1000$ were obtained by test runs at 700 K. The X^{tot} and \bar{X}^{gb} are the total solute concentration and GB solute concentration after hybrid MD/MC simulations, respectively.

$c_0 \times 100$, at. %	1	2	3	4	5	6	7	8	9	10
$\Delta\mu_0$	1.309	1.351	1.375	1.379	1.388	1.393	1.395	1.401	1.365	1.381
X^{tot} , at. %	1	2	3	4	4.9	5.9	6.9	8	9	10
\bar{X}^{gb} , at. %	3.8	7.7	11.4	14.7	17.6	20.3	22.6	24.9	26.5	28.4



Supplementary Fig. 1 Comparison of prediction errors between (a) without and (b) with linear simplification in additional solute-solute interactions in Al-Mg at 300, 400, and 500 K, respectively.



Supplementary Fig. 2 Solute distributions after hybrid MD/MC simulations in Ag-Ni 10 at.%, at (a) 300 K, (b) 500 K, and (c) 700 K, respectively. The green spheres are face-centered cubic (FCC) atoms, while the gray ones denote the GB atoms. The navy spheres represent Ni atoms. It shows that almost all the Ni atoms as clusters segregate to GBs after hybrid MD/MC simulations at different temperatures. These solute atoms concentrate at high-order junctions.